UNIVERSITY OF CALIFORNIA

RIVERSIDE

A Measurement of $t\bar{t}$ Production Cross Section in $p\bar{p}$ Collisions at $\sqrt{s} = 1.8$ TeV Using Neural Networks

A Dissertation submitted in partial satisfaction

of the requirements for the degree of

Doctor of Philosophy

in

Physics

by

Harpreet Singh

December, 1999

Dissertation Committee:

Professor Stephen Wimpenny, Chairperson

Professor John Ellison

Professor Richard Seto

Copyright by

Harpreet Singh

1999

The Dissertation of Harpreet Singh is approved:

Richard K. Lee

John A. [illegible]

Committee Chairperson

University of California, Riverside

This work is supported by the United States Department of Energy under the grant number DE-FG03-94ER40837.

I dedicate this dissertation to my parents who gave me life and dreams.

Acknowledgments

It is matter of great pleasure for me to reach somewhere in life where I can thank all the people who influenced my life in one way or other. I would like to express my particular thanks to my supervisor, Professor Stephen Wimpenny who has been guiding and generously supporting my efforts during graduate school. The stories of his intelligence, hard work and dedication always inspired me. I would also like to acknowledge his assistance in reading and correcting this manuscript.

Taste, experience and judgment in experimental high energy physics come slowly with time. Working in big experiment like DØ has been a fascinating experience for me. I am greatly indebted to my collaborators for building and operating the DØ detector and to all the staff of Fermilab for the excellent quality of their work in running the Tevatron. Many thanks to Professor P. Grannis, R. Raja, H. Montgomery and G. Fisk for their support.

My very special thanks go to Professor Jim Cochran for being a good friend and my advisor at Fermilab. I learnt a great deal from his knowledge and intuition about high energy physics. His patience in the pursuit of the beauty of physics have always been an example for me.

I am thankful to Professor J. M. Kohli, Dr. S. Beri and Dr. J. B. Singh of the high energy group at Panjab University where I started my research career. Thanks to the faculty and staff of Tata Institute of Fundamental Research, Mumbai for helping me learn detector hardware.

I am greatly indebted to Dr. Pushpa Bhat and Professor Harrison Prosper for their everyday help in clearing my concepts for this analysis. Their contributions to Neural Network analyses in DØ are immeasurable. I am also thankful to Herb Greenlee for all the help he provided. I want to express my utmost gratitude to Professor Tom Ferbel for his comments on analysis and the wonderful St. Croix summer school. Special thanks to Dhiman Chakraborty for providing many useful suggestions and ideas.

At Riverside, I would like to thank Professor John Ellison, Ann Heinson and Krish Gounder for providing a rich environment for high energy physics research. I owe Mrs. Yvonne Ayers an incredible amount of thanks for the countless time she has helped me with administrative work, often putting aside her crushing workload. Also my fellow graduate students at Riverside, Martin and Patrick, have been great and supportive friends.

At Panjab, I have enjoyed the company of fellow students, Vipin and Raman. Many thanks to my friends Satish, Avinash and my M.Sc. class fellows Amit, Sanjay, Pardeep, Manish, Baldy, Yoga, Manu and Sunil for all the fun we shared.

During my stay at Riverside I met some wonderful people. I can't forget the time spent with Jason, Tabitha and Greg. I remember those days (nights) when we

studied for qualifying examinations and the day Tabitha cried when I left for Fermilab (that touched me a lot). Jason deserves a special mention here for being my beer/wine/whiskey buddy. I would also like to thank Tora, Esmeal, Brian, Michelle, Kim, Gretchen, Nils and Nick for being very good friends.

My stay at Fermilab was made enjoyable by lot of people. Mrinmoy, Bornali, Prem and Prajakta were always there for me and fed me with lots of good food. Mrinmoy and Sailesh always helped and shared their knowledge of physics with me. An advice from Brajesh was always valuable. Thanks to Dhiman, Shankar, Satyadev, Ashutosh, Jeff, Wendy, Emanuela, Frederic, Vishnu, Scot, John Rha and Suyong for keeping my spirits up. I very much appreciated the presence of my office neighbors Darien, Pierrick, Neeti, Steve and Matt.

I am thankful to my swimming coaches and water-polo team who taught me how to fight and win.

Finally, I would like to express my gratitude to my parents Jagdev and Ranjit, uncle Mohinder, aunt Amrit and my brothers Manjeet and Darshan for their love and support. I am also thankful to my sister Gurdip and brother Manjinder for their support. My parents have always encouraged and inspired me to achieve high in academics. This dissertation would not have been possible without them. My last special thank goes to my fiancee Navgeet who came as a new song in my life.

September, 1999 Harpreet Singh

Main Entry: **quark**
Pronunciation: kwôrk, kwärk
Function: *noun*
Etymology: coined by Murray Gell-Mann
Date: 1964
: Any of several elementary particles that are postulated to come in pairs (as in the up and down varieties) of similar mass with one member having a charge of + 2/3 and the other a charge of - 1/3 and are held to make up hadrons

Abstract of the Dissertation

A Measurement of $t\bar{t}$ Production Cross Section in $p\bar{p}$ Collisions at $\sqrt{s} = 1.8$ TeV Using Neural Networks

by
Harpreet Singh
Doctor of Philosophy, Graduate Program in Physics
University of California, Riverside, December, 1999
Professor Stephan Wimpenny, Chairperson

We present the results of a new measurement of the $t\bar{t}$ production cross section using $e\mu$ channel in $p\bar{p}$ collisions at $\sqrt{s} = 1.8$ TeV. This study corresponds to an integrated luminosity of 108.3 ± 5.7 pb^{-1} acquired by the DØ detector during the Fermilab Tevatron Collider Run I (1992-1996). By using neural network techniques instead of the conventional analysis methods, we show that the signal acceptance can be increased by 10% (for $m_t = 172$ GeV/c^2) while the background remains constant. Four $e\mu$ events are observed in data with an estimated background of 0.22 $\pm$ 0.14 corresponding to a $t\bar{t}$ production cross section of 9.75 $\pm$ 5.53 pb.

Contents

List of Tables **xiii**

List of Figures **xiv**

Preface **1**

1 The Riddle of Matter **3**
1.1 From Antiquity to the 20th Century 3
1.2 The Standard Model 5

2 The top quark **9**
2.1 Why do we need the sixth quark? 9
2.2 What is special about the top quark? 12
2.3 Production Mechanism 14
2.4 Calculations of the $t\bar{t}$ production cross section 16
2.5 Decay Kinematics 18
2.6 Experimental Signature 20
2.7 The $e\mu$ Channel 22
2.7.1 Signal Characteristics 22
2.7.2 Backgrounds 23

3 Experimental Apparatus **27**
3.1 The Tevatron, a particle accelerator 27
3.2 The DØ Detector 30
3.2.1 The DØ Coordinate System 32
3.2.2 The Central Detector 33
3.2.3 The DØ Calorimeters 36
3.2.4 The Muon Spectrometers 44
3.2.5 Trigger and Data Acquisition 44

4 Event Reconstruction and Particle Identification **50**
4.1 DØRECO . . . 50
4.2 Tracking and Vertex Finding . . . 51
4.3 Electron/Photon Reconstruction and Identification . . . 51
4.3.1 Reconstruction . . . 51
4.3.2 Electron Identification . . . 52
4.3.3 Electromagnetic Energy Resolution and the Absolute Energy Scale . . . 55
4.4 Muon Reconstruction and Identification . . . 55
4.4.1 Reconstruction . . . 56
4.4.2 Muon Identification . . . 56
4.5 Jet Reconstruction and Identification . . . 58
4.5.1 Reconstruction . . . 58
4.5.2 Jet Identification . . . 58
4.5.3 Jet Energy Corrections . . . 59
4.6 Missing Transverse Energy ($\not\!\!E_T$) . . . 59

5 Analysis Tools **61**
5.1 Artificial Neural Networks . . . 61
5.2 The Neural Network as a Multivariate Classifier . . . 62
5.3 A Mathematical Model of the Neural Network . . . 63
5.3.1 Learning/Training of the Perceptron . . . 65
5.4 The Neural Network Package . . . 67
5.5 Neural Network Architecture and Learning Parameters . . . 67
5.5.1 Hidden Layers and Hidden Nodes . . . 67
5.5.2 Number of Training Cycles . . . 69
5.5.3 Learning Rate (η) . . . 69
5.5.4 Momentum Parameter (α) . . . 69
5.5.5 Inverse Temperature (β) . . . 69

6 Data Collection, Detection Efficiencies and Monte Carlo Simulations **70**
6.1 Data Collection . . . 70
6.1.1 Integrated Luminosity and Data Sample . . . 70
6.1.2 Triggers . . . 71
6.1.3 Preliminary Data Reduction . . . 71
6.2 Particle Selection and Detection Efficiencies . . . 72
6.2.1 Electron Selection and Identification Efficiency . . . 72
6.2.2 Electron Misidentification or 'Fake Electron' Rate . . . 73
6.2.3 Muon Selection and Detection Efficiency . . . 73
6.2.4 Trigger Efficiencies . . . 75

6.2.5 Combined Trigger and Particle Identification Efficiencies . . . 75
6.3 Monte Carlo Simulations . . . 76
6.3.1 Event Generation . . . 76
6.3.2 Detector Simulation . . . 77
6.4 $t\bar{t} \to e\mu$ Modeling . . . 78
6.5 Background Modeling . . . 78

7 Event Selection and Data Analysis 79
7.1 Neural Network Architecture . . . 79
7.1.1 Network Training . . . 79
7.1.2 Testing . . . 80
7.2 Event Selection and Data Analysis . . . 88
7.3 Acceptance and Event Yield Calculations . . . 96
7.4 Cross Section Calculations . . . 98
7.4.1 Systematic Uncertainties . . . 100
7.5 Results . . . 101

8 Comparison of the Neural Network and Conventional Analyses 103
8.1 The Published DØ $t\bar{t} \to e\mu$X Analysis . . . 103
8.2 Comparison of the Selection Efficiencies and the Cross Section Results 106

9 Conclusions 113

A Triggers used for Data Collection 115
A.1 Main Ring Triggers Definitions . . . 115
A.2 The L1 and L2 Triggers Definitions . . . 116

B The Branching Ratios for $t\bar{t} \to l_1 l_2$X Decays 117

C The properties of the Four Candidate Events 119

D Combining Neural Networks 126

Bibliography 128

List of Tables

1.1 The particles of the Standard Model-the Fermion Sector 7
1.2 The particles of the Standard Model-the Boson Sector 7
2.1 Calculations of $\sigma_{t\bar{t}}$ at $\sqrt{s} = 1.8$ TeV for $m_t = 175$ Gev/c^2. 19
2.2 Decay modes and their branching fractions for a $t\bar{t}$ pair. Note that all the branching fractions are calculated assuming $V_{tb} \simeq 1$. 21
3.1 Parameters of the Fermilab Tevatron collider for Run 1 (1992-1996). . 29
3.2 The operating parameters of the VTX chamber. 35
3.3 Some parameters of the CDC chamber. 37
3.4 Forward drift chamber parameters. 38
3.5 CC design parameters. 41
3.6 The design parameters of the ECN and ECS calorimeters. 43
3.7 Muon System Parameters. 45
6.1 Triggers for Run 1 71
6.2 Electron identification efficiencies for Run 1 72
6.3 Electron fake rate 73
6.4 Muon selection criteria 74
6.5 Muon identification efficiencies for Run 1a, 1b and 1c 74
6.6 Trigger efficiencies for Run 1 75
6.7 Trigger $\times$ identification efficiencies as a function of detector region and running period. 76
7.1 The expected and observed number of events as a function of cuts . . 95
7.2 Acceptance after all the cuts for different number number of interactions. error are statistical only. 98
7.3 Sources of systematic errors 100
7.4 Expected number of events, Efficiency times BR (%) and Total background for Run1 neural network analysis 102
8.1 The expected and observed number of events as a function of conventional cuts. 104
8.2 Event yields for the signal, background and data for the Run 1 conventional analysis 105
B.1 Branching ratios for $t\bar{t} \to ee$ or $e\mu$ or $\mu\mu$ including all the decays like $\tau \to e$ or μ 118

List of Figures

2.1 Feynman diagrams for $e^+e^- \to b\bar{b}$ via γ and Z exchange. 10
2.2 Feynman diagram for $Z \to b\bar{b}$. 10
2.3 An example of the fermion diagram which give rise to chiral anomalies in the Standard Model; f is a fermion, Q_f is a fermion charge, g_a^f is fermion axial coupling to Z. 11
2.4 The Standard Model particle masses on logscale. 12
2.5 Diagram of radiative corrections to $W^\pm$ and Z bosons with top quark and Higgs boson in virtual loops. 13
2.6 The dependence of the Higgs boson mass (bands from 90 to 1000 GeV/c^2) on the top quark mass (x axis) and the W boson mass (y axis). The contours represent the 68% (1σ) confidence level measurements. 14
2.7 Feynman diagram for lowest-order $t\bar{t}$ production. 15
2.8 Fractional contributions of $q\bar{q}$ (dashed) and gg (dotted) NLO processes to the production of $t\bar{t}$ at $\sqrt{s} = 1.8$ TeV. 16
2.9 Feynman diagram for s-channel single top quark production. 17
2.10 Feynman diagram for single top quark production via W-gluon fusion. 17
2.11 The $t\bar{t}$ and $t(\bar{t})$ production cross sections as a function of m_t at $\sqrt{s} =$ 1.8TeV. 18
2.12 The Standard Model decay of the top quark. 20
2.13 A pie chart showing the relative cross sections for various decay channels of a $t\bar{t}$ pair. 21
2.14 Schematic of the $t\bar{t} \to e\mu$X decay. 23
2.15 Lowest-order diagram for $\tau^+\tau^-$ production with Z or γ^* propagator. . 24
2.16 Lowest-order diagram for the Drell-Yan production of WW pairs. . . 24
2.17 Cartoon of the instrumental fakes for W+jets and QCD events, where at least one jet in the event is misidentified as an electron. 25
3.1 Schematic of the Fermilab accelerator complex. 28
3.2 A cut-away isometric view of the DØ detector. 31
3.3 The DØ coordinate system. 32
3.4 A side view of the DØ central tracking system. 34

3.5 A rϕ view of one quadrant of the VTX detector 35
3.6 A end view of the 3 CDC modules. 37
3.7 An exploded end view of the FDC. 38
3.8 A cut-away view of the CC and EC calorimeters. 40
3.9 A schematic of one quadrant of the Calorimeters showing arrangement of cells and towers. 40
3.10 A calorimeter unit cell showing the arrangement of the absorber plate, argon gaps and readout boards. 41
3.11 A view of the EC EM module. 43
3.12 The nuclear interaction length of the DØ detector as a function of the polar angle (θ). 45
3.13 An elevation view of the DØ detector showing the muon system. . . . 46
3.14 Block diagram of the Level 2 trigger and data acquisition system at DØ. 48
4.1 Various quantities used in electron identification (a) EM fraction (f_EM) (b) χ^2 (c) Track match significance (σ_{trk}) (d) Ionization (dE/dx) (e) TRD efficiency (ϵ_t) (f) Isolation ($\mathcal{I}$) (g) 4 variable likelihood (L_4) (h) 5 variable likelihood (L_5). The unshaded distributions are from electrons in $Z \to ee$ and $W \to e\nu$ events and shaded distributions are from electro-magnetic clusters in inclusive jet data. 54
5.1 A drawing of a neuron. 62
5.2 An elementary perceptron 64
5.3 A sigmoid function 65
5.4 A feed forward neural network with one hidden layer 65
5.5 Relative significance (signal/background) for various network parameters (a) Number of Training cycles, (b) Learning Rate η, (c) Momentum Parameter α and (d) Inverse temperature $\beta = 1/\mathrm{T}$ 68
7.1 Distributions of the variables used in NN1 81
7.2 The architecture of NN1 after training on instrumental background and $t\bar{t}$ events. The thickness of lines and size of the nodes represent the connecting strengths between different nodes and thresholds respectively. 82
7.3 Distributions of the variables used in NN2 83
7.4 The architecture of NN2 after training on WW and $t\bar{t}$ events. The thickness of lines and size of the nodes represent the connecting strengths between different nodes and thresholds respectively 84
7.5 Distributions of the variables used in NN3 85
7.6 The architecture of NN3 after training on Z$\to$ $\tau\tau$ and $t\bar{t}$ events. The thickness of lines and size of the nodes represent the connecting strengths between different nodes and thresholds respectively . . . 86
7.7 Schematic of the combined architecture 87

7.8 A plot of signal efficiency and background efficiency for a grid search on the $O_{NN1}, O_{NN2}, O_{NN3}$ and their combination O_{NN}^{comb}. Each circle is a set of cuts on $O_{NN1}, O_{NN2}, O_{NN3}$ 89
7.9 The distribution of total background and signal as a function of O_{NN}^{comb}. 90
7.10 The distribution of different backgrounds and signal as a function of O_{NN}^{comb}, Z $\rightarrow \tau\tau \rightarrow e\mu$, $WW \rightarrow e\mu$, $\gamma^* \rightarrow \tau\tau \rightarrow e\mu$ and QCD fakes . . . 91
7.11 The distribution of signal as a function of O_{NN}^{comb} for (a) $m_t = 150$ GeV (b) $m_t = 155$ GeV (c) $m_t = 160$ GeV (d) $m_t = 165$ GeV 92
7.12 The distribution of signal as a function of O_{NN}^{comb} for (e) $m_t = 170$ GeV (f) $m_t = 175$ GeV (g) $m_t = 180$ GeV (h) $m_t = 185$ GeV 93
7.13 The relative significance ($\frac{S}{\sigma_B}$) versus neural network output (O_{NN}^{comb}), where σ_B is the uncertainty on the estimated background. 94
7.14 Distributions of the signal, background and data as a function of neural network output. 96
7.15 (a) Acceptance and number of interactions; (b) Number of interaction in collider data 99
8.1 Comparison of signal and background efficiencies for the conventional and neural network cuts. 107
8.2 $\not{E}_T^{cal}$ and H_T^e scatter plots for signal and background (a) before any cuts (b) after neural network cut. The solid lines indicate the cut values used in the conventional analysis. 108
8.3 Comparison of the neural network and conventional $t\bar{t} \rightarrow e\mu$X analysis for Run 1 (a) Acceptance ($\mathcal{E}$). (b) Ratio of NN to conventional analysis efficiency (c) Expected number of events. The errors shown are statistical only. 109
8.4 Probability distributions verses m_t for the four $e\mu$ candidates. 110
8.5 The $t\bar{t}$ production cross section as measured using the $t\bar{t} \rightarrow e\mu$X channel. Also shown are NLO QCD calculations from Berger, Laenen and Catani *et. al.* The solid point is the result from this analysis and the open point is an updated version of the result using the published conventional analysis. 112
C.1 Event displays of event 58796/7338 (Run 1a, event 417) 122
C.2 Event displays of event 84676/12814 (Run 1b) 123
C.3 Event displays of event 90422/26920 (Run 1b) 124
C.4 Event displays of event 90834/5566 (Run 1b) 125

Preface

In fundamental research, the most basic question one can ask is "What is matter made up of?" Had no one asked this question, or similar ones, we would not now have transistors, the laser, nuclear energy and many other practical developments. Researchers worked long and hard, merely to satisfy their scientific curiosity. Much of their work has consisted of breaking open matter just to see what is inside, and perhaps grinding it up for a good measure. This scientific curiosity gave birth to High Energy Physics, which is more commonly referred to as Particle Physics.

Intensive and vigorous research in the past few decades by scientists throughout the world has resulted in tremendous advancement in this field. The study proceeds by probing the structure of matter, from molecules to atoms to nuclei to proton/neutron to quarks. The most powerful microscopes is still far above even the size of atom. In order to reach down into the interior of the nucleus, we need "microscopes" which can resolve objects which are as close as 10^{-13} cm apart. High energy particles from cosmic rays and particle accelerators are the only things which can penetrate into this sub-nuclear domain. The first particle accelerators built in 1930's were very different in size and capability from their modern counterparts. Today these machines are huge in size, often miles in length, and they are high in cost both in terms of money and the highly skilled technical manpower needed to run them.

This dissertation is devoted to the analysis of High Energy Physics data collected at Fermi National Accelerator Laboratory (Fermilab) with the D-Zero (DØ) detector. The Fermilab accelerator is the most powerful particle accelerator in the world. It consists of two rings of conventional and super-conducting magnets, four miles in circumference, which are used to collide highly relativistic beams of protons and anti-protons. Collisions occur at two points in the accelerator ring, each of which is surrounded by a massive piece of detection apparatus, which is used to study the results of these collisions. The DØ detector, located at one of the collision points is a multipurpose collider detector with almost 4π coverage. This is maintained and operated by an international collaboration of 400 physicists from 45 institutes around the world.

The DØ apparatus was designed to explore an energy regime which had not been explored in earlier experiments. Its goals were to search for the evidence of

new massive particles and to test the modern theory of particle physics known as the Standard Model. A major triumph came in 1995 when DØ experiment together with the CDF experiment (situated at the second interaction region at Fermilab) made the joint announcement of the discovery of a new quark, known as the top quark.

The subject of this dissertation is a measurement of the production cross section of the $t\bar{t}$ pairs at $\sqrt{s} = 1.8$ TeV. The analysis used artificial neural network logic instead of the conventional methods used in previous studies. These are multivariate analysis tools with the potential to give excellent signal to background discrimination in complex environments. They have been used previously with great success in the analyses of large cross section processes and for particle identification. This is the first analysis to attempt their application to the dilepton decays of a $t\bar{t}$ pair.

The dissertation is arranged as follows. Chapter 1 gives a brief introduction to the field of High Energy Physics and a sketch the present day theory of the fundamental particles and forces of nature. Chapter 2 focuses on the significance of the top quark and how it is produced and decays in the $p\bar{p}$ environment. This chapter discuss the signal and relevant background to the production of $t\bar{t}$ process studied for this dissertation. Chapter 3 gives a brief overview of the Fermilab accelerator complex and the apparatus at DØ where the measurements were performed. Chapter 4 describes the process of event reconstruction and particle identification. The basic concepts and theorems of neural networks are discussed in Chapter 5. In Chapter 6, we define the data samples, detection efficiencies and Monte Carlo simulations used in our study. In Chapter 7, we explain the training and optimization of neural networks we used in the study and describes the neural network analysis. Chapter 8 compares the results of this analysis to the conventional style analysis. Finally, Chapter 9 summarizes the results and conclusions of the study.

Chapter 1

The Riddle of Matter

...This supreme science was thus received through the chain of disciplic succession.

- Bhagavad Gita

1.1 From Antiquity to the 20th Century

Some tens and thousands of years ago, when ancient man created tools for his needs, he had to experiment with various materials and configurations, such as different kinds of wood and stone for bows and arrows and useful arrangements for traps to achieve success. Thus, it was necessary that he perform research tasks to satisfy certain needs. His curiosity motivated him to accumulate information from observations and this led him to ask questions such as why the universe exists and of what it is made up of.

The ancient Indians, believed in five elements: space, earth, air, fire, and water. Likewise, the ancient Chinese counted five fundamentals: earth, wood, metal, fire, and water. Similarly, ancient Greeks chose: air, fire, water, and earth as the four basic elements. At some point, people began to think that things were made up of microscopic particles called atoms. About 600 B.C., an Indian philosopher named Kanada formulated some ideas about the atom. These were further pursued by the Greek philosophers Leucippos and Democritus (about 400 B.C.), who argued that everything consists of tiny atoms - a bone is made of bone-atoms, wood is made of wood-atoms, and so on. Much later, scientists began to understand some of the underlying patterns to the structure of matter and the field of chemistry was born. Atoms (not Democritus's kind) were first grouped into a periodic table by Dmitri Mendeleyev between 1869 and 1871. By arranging the elements in a specific way, many of their physical and chemical properties could be predicted quite accurately.

By the end of the nineteenth century it was recognized that the atoms of

chemical elements were not indestructible and could be modified or perhaps even broken up if heated enough. The problem was to find right method of heating atoms. The answer was found in the newly discovered science of electricity. German physicists, Plücker, Hittorf and Goldstein learnt to pull atoms apart into two components by causing electric discharge in low-pressure gases. J. J. Thomson in England then studied the two parts and found in 1897 that one part consists of negatively charged particles called electrons.[1] He identified the other component as positively charged particles more massive than the electron. The lightest of these heavy positive particles, called the proton, is the heavy part of the hydrogen atom.

In 1911, Ernest Rutherford showed from his experiments that the heavy positive part is the center of the atom (nucleus) and it is surrounded by a number of negatively charged particles (electrons) which orbit around it and are bound to it by the electro-magnetic force. Soon afterwards, the Danish physicist Niels Bohr built a mathematical description of the atom using the Planck's theory of quantization of energy. In his model, electrons move around the nucleus in fixed orbits and can only switch between orbits when a certain discreet amount of energy is absorbed or emitted. This amount of energy is the energy of the photon of specific wavelength. The picture of atom became more transparent, when Heisenberg in Germany predicted that a neutral heavy counterpart of the proton should exist. In 1932, Chadwick in England discovered this particle which he called the neutron.

The existence of positron (e^+) was predicted by Paul Dirac in 1928. This is the anti-particle of electron- a particle with the same mass but opposite electric charge. This was established in experimentally 1933 and was followed shortly afterwards in 1938 by another charged particle, the muon (μ) which has mass 206 times larger. The energy loss problem in radioactive β decay was solved by the Italian, Enrico Fermi, who predicted a new particle called the neutrino, which was later observed in 1947 in cosmic ray experiments.

By the middle of twentieth Century, only a few elementary particles namely the electron, proton, neutron, photon, muon and neutrino were known. These are the building blocks of our universe. However, the study of cosmic rays and the nuclear force led to the inference of new elementary particles which were not needed to build matter. This led to the construction of particle accelerators and the subsequent observation of many hundreds of new particle states. These states were called "hadrons", meaning heavy, and were further divided into lighter "mesons" and heavier "baryons".

The increasing number of hadrons suggested that there was something more fundamental than the hadrons. In 1964, Murray Gell-Mann and George Zewig proposed the static quark model [1]. In this picture the hadrons are made out of three more fundamental constituents called *quarks*, which come in three types called up,

[1] The existence of the electron and the name had been first suggested by Stoney in 1874, also in England.

down and strange (u,d and s). The quarks are believed to be bounded together inside the hadrons by the exchange of quanta of strong interaction known as "gluon". The static quark model was very successful in explaining the known "hadronic" particle states. It was further supported by the first results from a new accelerator at SLAC in the early 1970s which demonstrated the existence of a internal structure to the proton and neutron.

In 1974, a new particle called the tau (τ) was discovered at SLAC. This together with electron (e), muon (μ) and three corresponding types of neutrinos (ν_e, ν_μ, ν_τ[2]) form a different family of the fundamental particles which are collectively known as *leptons*. The charged leptons interact via the electro-magnetic and weak interactions, while neutrinos are distinguished by having only weak interactions. The unification of electro-magnetic and weak interactions by Weinberg, Glashow and Salam [2] predicted the existence and masses of the bosonic particles (W^+, W^- and Z^o) believed to be the mediators of electroweak force. This picture was verified in 1984 when these particles were discovered by the CERN S$\bar{p}p$S collider experiments UA1 and UA2 [3].

Since the static quark model was proposed, three more quarks have been discovered, the charm (c) quark in 1974, the bottom (b) quark in 1977 and the top (t) quark in 1995 [4]. The theoretical picture that describes how these elementary particles are organized and how they interact with one another via the forces is known as the Standard Model.

1.2 The Standard Model

Over the last century the field of particle physics had developed through the efforts of experimentalists and theorists. The physical world we live in, is governed by four fundamental forces:

1. Electro-magnetic force
2. Weak force
3. Strong force
4. Gravitational force

High energy physics is concerned with the first three of these. Gravity is so much weaker than the other three that it has no influence on subatomic processes and can be excluded from the following discussion.

There are two basic types of particles in the Standard Model: fermions and bosons. The fermions have spin $\frac{1}{2}$ and are the building blocks of matter. These adhere to the Pauli Exclusion principle so that only one fermion can occupy a particular quantum state. The bosons are either spin 0 or 1 particles and are believed to be the carrier of the force between the particles. The fermionic constituents in

[2] ν_τ has not been directly observed yet.

the Standard Model are further divided into quarks and the leptons. The leptons interact via electro-magnetic and weak force and the quarks engage in the strong interaction as a consequence of their color charge.[3]

In the case of the strong and electro-magnetic interactions the bosons are massless whereas the weak interaction they are quite massive ($M_W \approx 80$ GeV, $M_Z = 91$ GeV). The eight gluons (strong interaction), the photon (electro-magnetic) and the W and Z (weak interaction) are assumed to be elementary. There is no experimental evidence for quark and lepton compositeness, such as excited states and form factors and so these are also assumed to be the fundamental particles.

Table 1.1 and Table 1.2 summarize the properties of the particles of the Standard Model. Mass values are in units of GeV/c^2 and electric charges are given as multiples of the proton charge e.

The Standard Model Lagrangian embodies our knowledge of the strong and electroweak interactions. It contains as fundamental degrees of freedom: the quarks and leptons, the spin 1 gauge bosons and a spin 0 Higgs field.[4] Symmetry plays the central role in determining its dynamical structure. The Lagrangian exhibits invariance under $SU(3)$ gauge transformations for the strong interactions and under the $SU(2) \otimes U(1)$ gauge transformations for the electroweak interactions. Thus, the gauge group for the Standard Model is $SU(3)_C \otimes SU(2)_L \otimes U(1)_Y$ [5].

The weak isospin complex doublet of spin-zero Higgs fields $\Phi = \binom{\phi^+}{\phi^0}$ with the potential function:

$$V(\Phi) = \mu^2(\Phi^\dagger\Phi) + |\lambda|(\Phi^\dagger\Phi)^2. \tag{1.1}$$

breaks the electroweak and flavor symmetry in the Standard Model. Here λ is the self interaction(coupling) of the Higgs scaler field. Mass generation for fermions and gauge bosons proceeds by means of spontaneous breaking of the $SU(2)_L \otimes U(1)_Y$ symmetry. The potential V of Equation 1.1 is minimized to obtain ground state Higgs configuration.

$$\Phi(\mu^2 + 2\lambda\Phi^\dagger\Phi) = 0 \tag{1.2}$$

The Equation 1.2 has two solutions, the trivial solution $\langle\Phi\rangle_0 = 0$ and the nontrivial solution

$$\langle\Phi^\dagger\Phi\rangle_0 = -\frac{\mu^2}{2\lambda} = \frac{v^2}{2} \tag{1.3}$$

with

$$v = \sqrt{\frac{-\mu^2}{\lambda}} \tag{1.4}$$

[3]Each quark carries a quantum number called color, There are three such quantum numbers namely red, blue and green

[4]Higgs boson is not observed yet.

[5]C is the color quantum number, L denotes left handed group and Y is the hypercharge.

Generation	Particle Name	Mass (GeV/c^2)	Charge (e)	Force
	Quarks (spin 1/2)			
1	Down (d)	0.005	$-1/3$	Strong, EM, Weak
	Up (u)	0.01	$2/3$	Strong, EM, Weak
2	Strange (s)	0.2	$-1/3$	Strong, EM, Weak
	Charm (c)	1.5	$2/3$	Strong, EM, Weak
3	Bottom (b)	4500	$-1/3$	Strong, EM, Weak
	Top (t)	173.8	$2/3$	Strong, EM, Weak
	Leptons (spin 1/2)			
1	Electron (e)	5.1×10^{-4}	-1	EM, Weak
	Electron neutrino (ν_e)	$< 0.8\times10^{-8}$	0	Weak
2	Muon (μ)	0.105	-1	EM, Weak
	Muon neutrino (ν_μ)	$< 2.7\times10^{-4}$	0	Weak
3	Tau (τ)	1.777	-1	EM, Weak
	Tau neutrino (ν_τ)	< 0.035	0	Weak

Table 1.1: The particles of the Standard Model-the Fermion Sector

Particle	Name	Mass (GeV/c^2)	Charge (e)	Force
Gauge Bosons (spin 1)				
γ	Photon	0	0	Electro-magnetic
g	Gluon	0	0	Strong
W	W	80.2	1	Weak
Z	Z	91.2	0	Weak
Fundamental Scalar (spin 0)				
H	Higgs	?	?	Couples to matter

Table 1.2: The particles of the Standard Model-the Boson Sector

Choosing μ^2 to be negative would make the nontrivial solution of Equation 1.3 real and this equation not only respects the conservation of charge but also spontaneously breaks the $SU(2)_L \otimes U(1)_Y$ symmetry.

A consequence of the spontaneous breaking of the electroweak symmetry is that the $W^{\pm}$ and Z^0 acquire mass according to:

$$M_W^2 = \frac{\pi\alpha}{G_F\sqrt{2}\sin^2\theta_W} \tag{1.5}$$

$$M_Z^2 = \frac{M_W^2}{\cos^2\theta_W} \tag{1.6}$$

whereas photon remains massless ($M_\gamma = 0$). This also gives rise to a spin 0 (scalar) particle called the Higgs boson. In Equation 1.5, G_F is the Fermi (weak) coupling constant, α is the fine structure constant and θ_W is the weak mixing angle. Each of the fermions (f, lepton and quark) has its own Yukawa coupling (G_f) to the Higgs boson. Thus, the fermion mass is given by

$$m_f = \frac{v}{\sqrt{2}}G_f \tag{1.7}$$

The value of v is given by $v = \sqrt{-\mu^2/\lambda} = (G_F\sqrt{2})^{-\frac{1}{2}} = 246$ GeV. Although the theory can accommodate fermions of any mass, it does not predict the mass values. Instead, the measured fermion masses are used to fix the arbitrary Higgs-fermion (Yukawa) coupling.

The Standard Model has been extremely successful so far [5]. Despite intense experimental scrutiny, this theory has displayed no experimental inconsistencies. However, the Standard Model does have several features which many physicists consider unsatisfactory. There exists no understanding of the number of families and the presence of so many free parameters (nine fermion masses, three coupling coefficients, four CKM matrix elements and one Higgs boson mass). Hence, physics beyond the Standard Model seems inevitable [6]. The mass of the top quark [7] suggests that its Yukawa coupling (G_f) to Higgs boson is ~ 1 (see Equation 1.7). It is quite possible that the top quark might provide a window to the new physics.

Chapter 2

The top quark

The truth is out there.

- The X-files

2.1 Why do we need the sixth quark?

The tau lepton (τ) was the first particle of third generation particles to be discovered [8]. Shortly afterwards, the Υ was discovered at Fermilab as a resonance in the $\mu^+\mu^-$ invariant mass spectrum [9]. This was interpreted as a $b\bar{b}$ bound state which subsequently decays into $\mu^+\mu^-$. The bottom (b) quark is a third generation quark. In the past few years a tremendous amount of experimental data on its properties has been collected. Both its charge ($Q_b = -\frac{1}{3}$) and isospin ($I_3 = -\frac{1}{2}$) are well established.

The first measurement of the charge of the b quark was done by measuring the leptonic width of the Υ resonance at the DORIS e^+e^- storage ring [10]. The Υ leptonic width is proportional to the square of the charge of the b quark. From these measurements, it was found to be $Q_b = -\frac{1}{3}$.

The weak isospin of the b quark was first determined from the measurement of forward-backward asymmetry (A_{FB}) in $e^+e^- \to b\bar{b}$ production. The definition of the asymmetry in terms of the production cross section (σ_b) is:

$$A_{FB} = \frac{\sigma_b(\theta > 90^o) - \sigma_b(\theta < 90^o)}{\sigma_b(\theta > 90^o) + \sigma_b(\theta < 90^o)} \tag{2.1}$$

where θ is the polar angle of the quark in the e^+e^- center of mass as measured from the direction of the e^-.

The production of $b\bar{b}$ pairs in e^+e^- collisions can be either mediated by a photon (γ) or a Z boson (see Figure 2.1). The contributions of the photon (γ) exchange to the angular distributions are symmetric. An asymmetry arises through

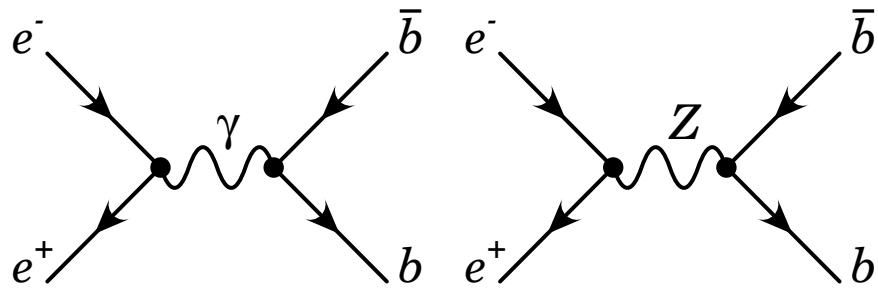

Figure 2.1: Feynman diagrams for $e^+e^- \to b\bar{b}$ via γ and Z exchange.

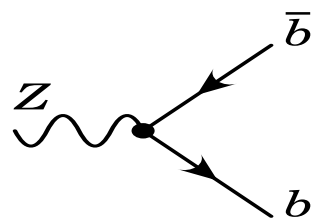

Figure 2.2: Feynman diagram for $Z \to b\bar{b}$.

the Z contributions (see Figure 2.2) because of the coupling of the Z boson to fermions, which depend on the weak isospins of the leptons. This arises through a term in the Lagrangian of the form $\bar{f}\gamma_\mu(g_V - g_A\gamma_5)Z^\mu f$, where γ_5, γ_μ are Dirac matrices, f is fermion field and g_V, g_A are the vector and axial couplings which are given by

$$g_V = 2[I_3^L(f) + I_3^R(f)] - 4Q_f \sin^2\theta_W \tag{2.2}$$

$$g_A = 2[I_3^L(f) + I_3^R(f)] \tag{2.3}$$

where $I_3^L(f)$ and $I_3^R(f)$ are the isospins for left-handed and right-handed fermion field, θ_w is the Weinberg angle and Q_f is the charge of the fermion.

The measurements of A_{FB} were found to be consistent with the Standard Model predictions assuming $I_3 = -\frac{1}{3}$ for the weak isospin of the b quark [11]. If the b quark is an $SU(2)$ weak-isospin singlet state, it cannot decay via the charge current (W) because it won't have charge current interactions. The other decay mode would be a flavor-changing neutral current (FCNC, $(b \to s(Z/\gamma) \to sl^+l^-)$. FCNC decays are suppressed for the isospin doublet quarks by GIM mechanism [12]. If the b quark is a isospin singlet state then FCNC decays should be observed at a rate well above the present experimental limits [13]. However, the charge current decay is readily observed leading to the conclusion that the b quark must be a member of

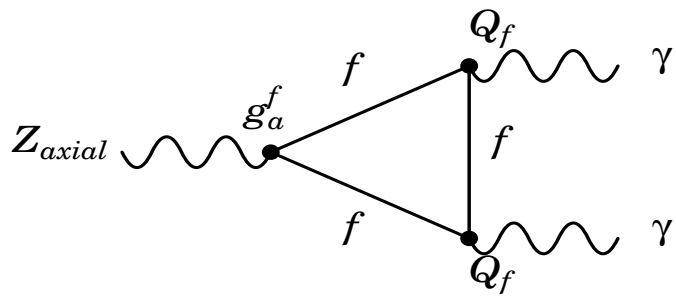

Figure 2.3: An example of the fermion diagram which give rise to chiral anomalies in the Standard Model; f is a fermion, Q_f is a fermion charge, g_a^f is fermion axial coupling to Z.

weak isospin doublet.

The establishment of a third generation isospin doublet implies the existence of an additional quark which is referred to as the top (or truth) quark (t). Furthermore, the renormalizablity of electroweak sector in the Standard Model requires cancellations of the triangle anomalies which arise from the diagram shown in Figure 2.3. The contribution of this diagram for each fermion is $n_c \times g_a^f \times Q_f^2$, where $n_c = 3$ for quarks. Equation 2.4 implies that the net contribution from a isospin doublet is zero, thereby avoiding the problem.

$$Q_f = -1 + 3 \times \left[\left(\frac{2}{3}\right) + \left(-\frac{1}{3}\right)\right] = 0 \tag{2.4}$$

There is other indirect experimental evidence which indicates the existence of top quark. The observed rate of $B_d^o - \bar{B}_d^o$ mixing is proportional to $\mid V_{td} \mid^2$, the Cabibbi-Kobayashi-Maskawa (CKM) matrix element for the t and d quark coupling [14, 15]. This implies that a massive top quark is needed in the loops so that the b quark can decay indirectly via an intermediate state containing a virtual t quark to the d quark. This indicates that the b quark has a weak isospin partner, the top quark with weak isospin $I_3 = +\frac{1}{2}$.

The precise measurements of Z width by experiments at the LEP and SLAC rule out the existence of fourth generation neutrino with a mass $M_\nu \leq M_Z/2$ [16]. Thus, unless the additional neutrinos are really massive, no additional generations in the Standard Model are allowed. Thus, the top quark is the last fermion expected in the minimal Standard Model.

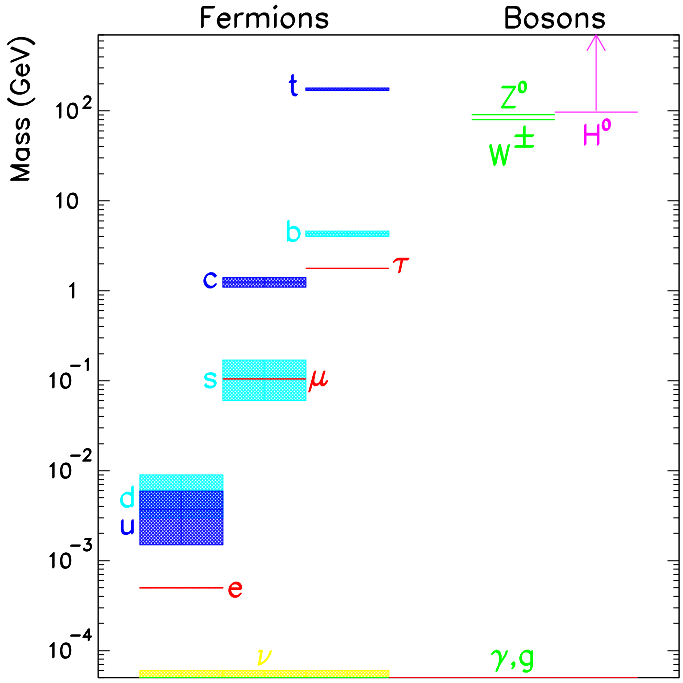

Figure 2.4: The Standard Model particle masses on logscale.

2.2 What is special about the top quark?

The Standard Model predicts the weak isospin ($I_3 = +\frac{1}{2}$) and charge ($Q_t = +\frac{2}{3}$) of the top quark but its mass remains as a free parameter in the model. The most recent measurements of the top quark mass yield $m_t = 174.3 \pm 5.1$ GeV/c^2 [17]. This a factor 40 higher than the mass of the b quark, the second heaviest fermion and almost a factor of two higher than the mass of the heaviest of the known bosons the Z^0. The masses of the particles of the Standard Model are shown in Figure 2.4. It is quite clear that its large mass sets the top quark apart.

The value of the top quark mass (m_t) enters in numerous calculations of radiative corrections to the electroweak sector in the Standard Model. The parameters α, G_F and θ_W determine the mass of weak vector bosons ($W^\pm, Z^0$) to the lowest order (see Equations 1.5, 1.6). However, the higher order radiative corrections such as those shown in Figure 2.5 depend on the mass of both the top quark and Higgs boson. One such correction is:

$$\Delta\rho = \frac{n_c g_2^2}{64\pi^2 M_W^2}\left[m_t^2 + \frac{M_W^2}{3}\left[\frac{11}{3}\ln\left(\frac{M_H^2}{M_W^2}\right) + \ldots\right] + \ldots\right] \tag{2.5}$$

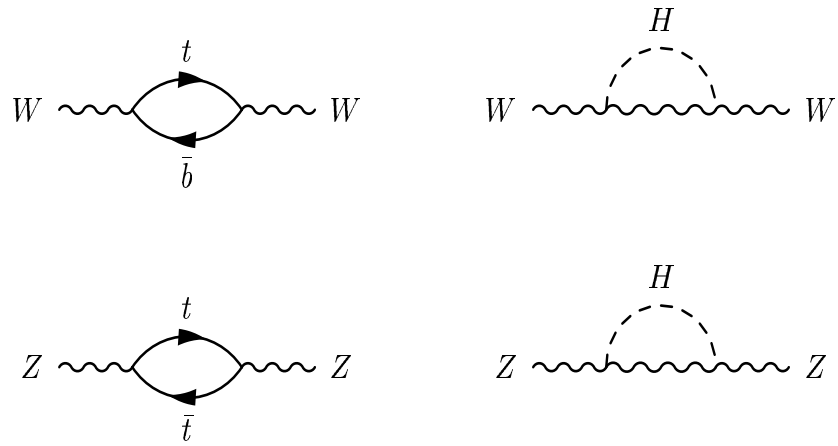

Figure 2.5: Diagram of radiative corrections to $W^{\pm}$ and Z bosons with top quark and Higgs boson in virtual loops.

where $n_c = 3$ and $g_2^2 = \frac{8G_F M_W^2}{\sqrt{2}}$. The dependence of this radiative correction is quadratic in the top quark mass whereas the dependence on Higgs boson mass is logarithmic. Because of the large value of m_t, the term containing m_t is the dominant parameter in the electroweak radiation corrections. Equation 2.5 was used to set the constrains on the top quark mass before it was measured directly. Today, since m_t has been measured, the argument has been reversed and used to test electroweak theory.

The electroweak sector of the Standard Model predicts the relationship between m_t and the masses of the W boson (M_W) and the Higgs boson (M_H). A precise measurement of m_t and M_W can be used to obtain constrains on the mass of the undiscovered Higgs. However, because of the logarithmic dependence of the M_H and the accuracy of the present measurements, this can only set a weak constraint on M_H. This is shown in the Figure 2.6, where the two ellipses represent direct (solid) and indirect (dashed) measurements. The shaded bands are the Standard Model predictions for M_H values between 90 and 1000 GeV.

The top quark production cross section can be calculated using the perturbative QCD. Thus, a precise measurement of the cross section would both test the predictive power of the theory and be sensitive to new physics in the form of enhancements to the $t\bar{t}$ production cross section. Such effects are predicted in the color octet, top color and technipion models [18, 19].

The decay of the top quark provides an opportunity to study the properties of a bare quark such as spin correlations [20] which are free from the long range effects of the strong interaction. In $p\bar{p}$ collisions $t\bar{t}$ pairs are produced via spin 1 boson (γ, Z^0, gluon) exchange. The decay time of the top quark ($\approx 10^{-25}$sec) is less

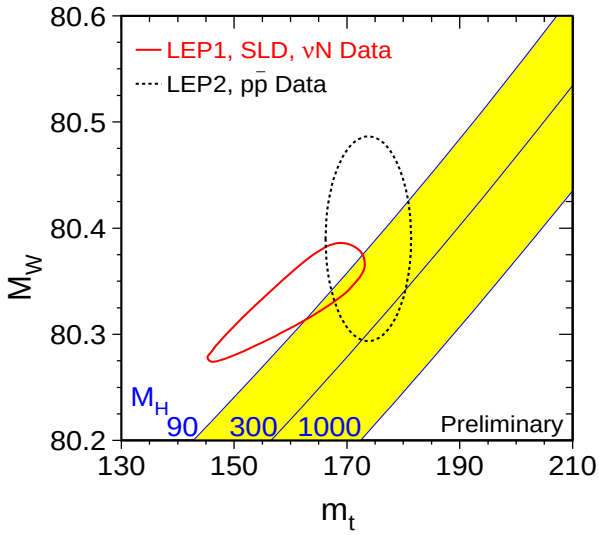

Figure 2.6: The dependence of the Higgs boson mass (bands from 90 to 1000 GeV/c^2) on the top quark mass (x axis) and the W boson mass (y axis). The contours represent the 68% (1σ) confidence level measurements.

than the QCD hadronization time-scale ($\approx 10^{-23}$sec). Thus, the spin correlation information is preserved and is reflected in the angular correlations of the decay products. Observing such correlations would confirm that the top quark has spin $\frac{1}{2}$ and that it decays before hadronizing, thereby giving a limit on the top quark lifetime. This could also be used to provide a lower bound on the CKM matrix element V_{tb} without imposing a three generation constraint [20].

Because of large mass of the top quark, it is quite possible that the new physics may manifest itself at the top decay vertex. Thus, the study of top quark production and decay is a excellent place to look for evidence of new particles such as stop, $\tilde{t}$ or charged higgs $H^{\pm}$ which exist in the extensions of the Standard Model. This can be done by comparing the ratios of the decays of the top quark with the Standard Model expectations. To date no such divergences have been observed.

The large top quark mass singles it out in several ways. It has a significant effect on electroweak physics and it may play a special role in the electroweak symmetry breaking.

2.3 Production Mechanism

Because of its large mass, the top quark can only be produced in the collisions of the particles where a sufficiently high center-of-mass energy ($\sqrt{s}$) can be achieved.

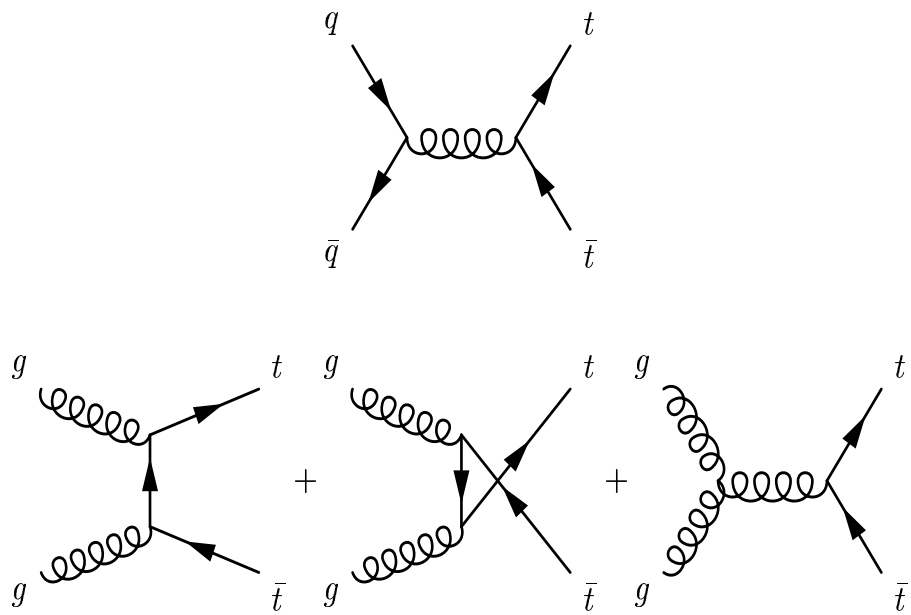

Figure 2.7: Feynman diagram for lowest-order $t\bar{t}$ production.

The proton-anti-proton ($p\bar{p}$) accelerator (the Tevatron) at Fermilab operating at $\sqrt{s}$ of 1.8 TeV is the only facility in the world where the top quarks can be and have been produced. It was here that the top quark was discovered in 1995 by the DØ and CDF experiments [4]. A new proton-proton (pp) collider called the LHC is under construction at the CERN laboratory at Geneva. With a center-of-mass energy of 14 TeV, this will be capable of producing the large number of top quark events when it comes on line in 2006. Top quark physics could also be pursued at other machines such as high energy e^+e^- and $\mu^+\mu^-$ colliders. However, these machines are still in the design stage and will not be available in the immediate future. For this dissertation, we focus on the features of the top quark production at Fermilab.

In $p\bar{p}$ collisions, there are two mechanisms for the top quark production. The pair production via strong interaction and single top production via electroweak interaction. These are discussed below:

1. Pair production of the top quarks ($t\bar{t}$ production):

Figure 2.7 shows the leading order processes which contribute to $t\bar{t}$ pair production at the Tevatron. At $\sqrt{s} = 1.8$ TeV, the $q\bar{q} \to t\bar{t}$ diagram dominates, contributing 90% of the total production cross section (see Figure 2.8). In principle, there are also $q\bar{q}$ diagrams with γ^* or Z^* propagators which could result in $t\bar{t}$ final states. However these are electroweak processes and the cross sections are much smaller.

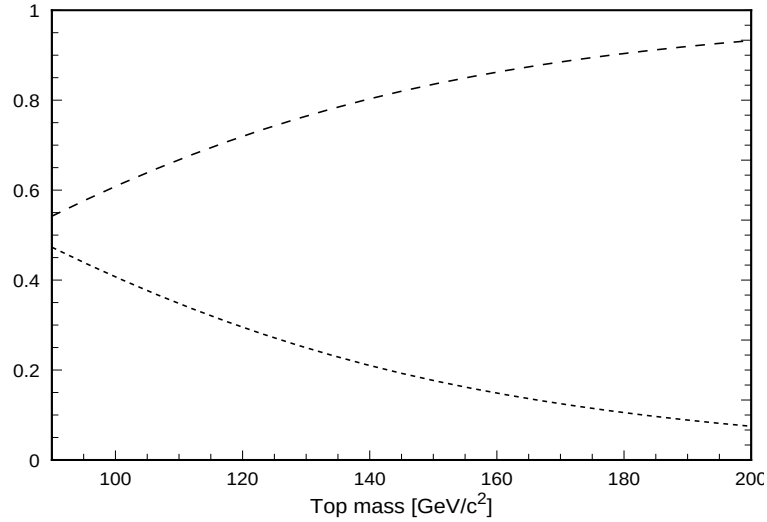

Figure 2.8: Fractional contributions of $q\bar{q}$ (dashed) and gg (dotted) NLO processes to the production of $t\bar{t}$ at $\sqrt{s} = 1.8$ TeV.

2. Single top quark production:

Single top quark production can occur through s, t or u-channel electroweak processes. At $\sqrt{s} = 1.8$ TeV, the dominant processes are s-channel production of a tb final state via off mass-shell W^* exchange and production of tqb final state via W-gluon fusion (see Figure 2.9). Although the single top production cross section is one third that of the $t\bar{t}$ production cross section [21], the detection efficiencies for single top quark events are lower and the signal is much more difficult to separate from the background. At this time there is no direct measurement of single top production cross section although some preliminary limits are available [22].

This thesis focuses on the study of the $t\bar{t}$ final state for which the detection efficiencies and the cross section are larger (see Figure 2.11).

2.4 Calculations of the $t\bar{t}$ production cross section

The production cross section for the $t\bar{t}$ process in $p\bar{p}$ collisions can be calculated in perturbative QCD. It can be written as a product of the parton distribution functions of the proton and the parton-parton point cross sections. This is then summed over all the contributions from the quark and gluon processes [23].

$$\sigma_{p\bar{p}\to t\bar{t}} = \sum_{a,b} \int dx_a F_a^p(x_a, q^2) \int dx_b F_b^p(x_b, q^2) \hat{\sigma_{ab}}(\hat{s}, q^2, m_t) \tag{2.6}$$

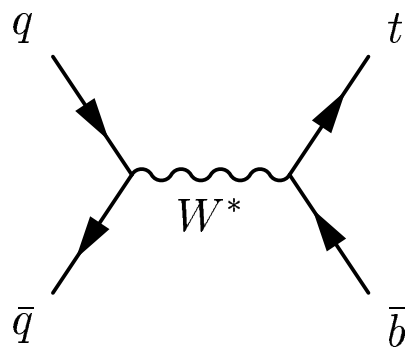

Figure 2.9: Feynman diagram for s-channel single top quark production.

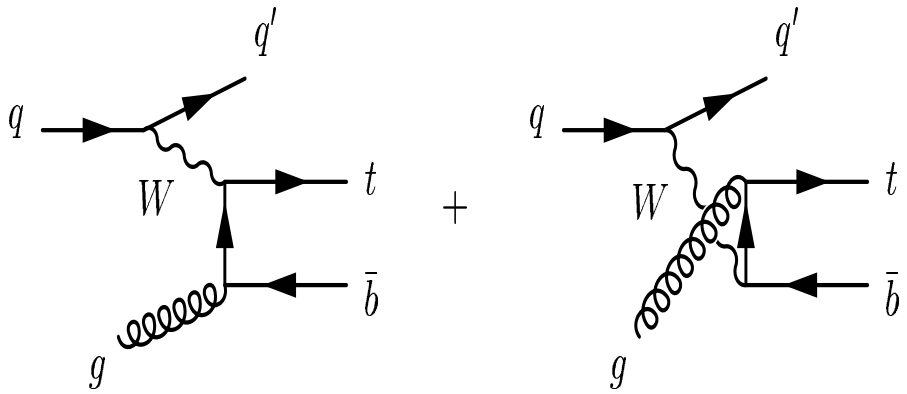

Figure 2.10: Feynman diagram for single top quark production via W-gluon fusion.

The functions F_a and F_b represents the probability densities of the light partons (u, d, s, c, b) which carry momentum fractions x_a and x_b respectively and are evaluated at scale q. $\hat{\sigma_{ab}}$ is the point cross section for the process $a + b \to t\bar{t}$ and $\hat{s} = 4x_a x_b$. While calculations to all orders of perturbative QCD would be independent of the choice of q, practical calculations are performed to a finite order so that the results can depend on the choice of the scale. This usually chosen to be $q \sim m_t$.

The first calculations of $\sigma_{t\bar{t}}$ in leading order (LO, $O(\alpha_s^2)$) were done in late 1970's [24]. About 10 years later, these were followed by the next-to-leading-order (NLO, $O(\alpha_s^3)$) calculations [25]. In perturbation theory, the NLO contribution should be small as compared to LO. However for $t\bar{t}$ production at the Tevatron the NLO contributions are still large because contributions from processes involving of soft gluon emission. This implies that still higher order calculations are needed to establish stability of the results. To incorporate these, a technique call *resummation* is used in which the dominant logarithms from soft gluon emission are calculated and summed to all orders in perturbation theory. This is problematic because the

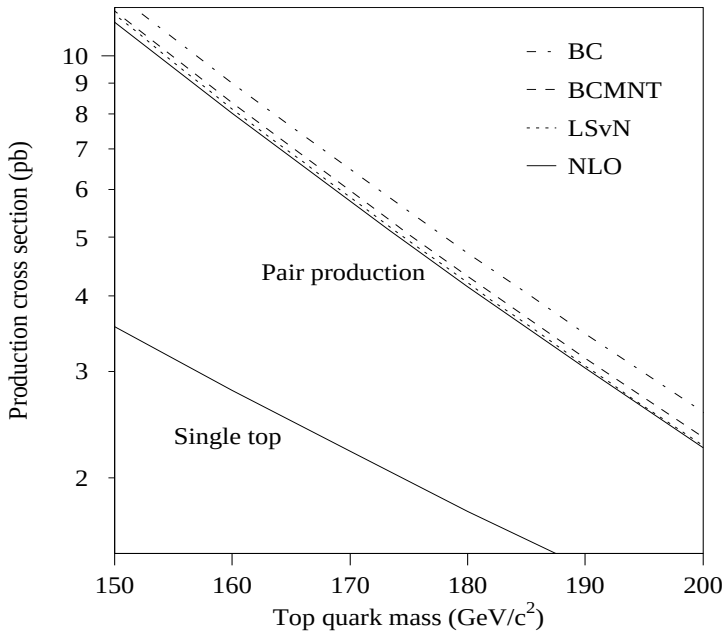

Figure 2.11: The $t\bar{t}$ and $t(\bar{t})$ production cross sections as a function of m_t at $\sqrt{s} =$ 1.8TeV.

re-summed series are divergent due to non-perturbative effects as α_s becomes large. The solution is to introduce a new scale, $q_0 >> \Lambda_{QCD}$, which can be used as a cutoff and removes the divergence. The first of these calculations were performed by Laenen, Smith and van Neerven (LSvN) [26]. Subsequent calculations was done using different techniques which avoid the need for the infrared cutoff, q_0 [27, 28]. Berger and Contopanagos (BC) [27] used a technique called principal value resummation (PVR) to include the resummation of gluon radiative correction, whereas Bonciani, Catani, Mangano, Nason and Trentadue (BCMNT) [28] used a slightly different scheme to avoid the divergence. A full discussion on the differences between these calculations are given in references [27, 28, 29] and the results are compared in Figure 2.11. Table 2.4 composes the results for $m_t = 175$ GeV and summarizes the main features of the calculations.

2.5 Decay Kinematics

According to Quantum Chromodynamics (QCD), quarks are confined and are not observed as free particles [31]. For $m_t = 175$ GeV/c^2 the decay width of

Calculation	PDF	Order	$\sigma_{t\bar{t}}(pb)$
Exact NLO (NLO)	MRSR2[30]	NLO only	$4.87^{+0.30}_{-0.56}$
Laenen, Smith and van Neerven (LSvN)	MRSD′[30]	NLO + gluon resummation	$4.94^{+0.71}_{-0.45}$
Berger and Contopanagos (BC)	CTEQ3[32]	NLO + gluon resummation	$5.52^{+0.07}_{-0.42}$
Bonciani, Catani, Mangano, Nason and Trentadue (BCMNT)	MRSR2[30]	NLO + gluon resummation	$5.06^{+0.13}_{-0.36}$

Table 2.1: Calculations of $\sigma_{t\bar{t}}$ at $\sqrt{s} = 1.8$ TeV for $m_t = 175$ Gev/c^2.

the top quark (Γ_{top}) is ≈ 1.8 GeV and its lifetime is $\simeq \frac{\hbar}{\Gamma_{top}} \simeq 10^{-25}$ seconds. In comparison, the hadronization time scale is of the order of $\approx 10^{-24}$ seconds. Since the lifetime of the top quark is shorter than the hadronization time scale, the top quark decays before the hadronization can take place.

Assuming the Standard Model couplings, the top quark decays to a b quark via W emission ($t \to W^+b$), where the W boson is real because $m_t > M_W^+ + m_b$. This is a weak flavor changing charge current (FCCC) decay. Other FCCC decays such as $t \to W^+s$ and $t \to W^+d$ are also allowed, but are suppressed by factors of $\approx 10^{-3}$ (for $t \to W^+s$) and $\approx 10^{-4}$ (for $t \to W^+s$) by the mixing elements of CKM matrix [15]. Super-symmetric models predict the existence of a pair of charge Higgs scalers ($H^\pm$) [34]. If $M_H^+ < m_t - m_b$ then the decay $t \to H^+b$ can also occur. Recent searches and the limits on the charged Higgs decay mode of the top quark can be found in reference [35]. Other decay modes such as flavor changing neutral currents (FCNC) are also predicted but are many orders of magnitude smaller in size [33]. These have branching fractions of BR($t \to cg$) $\sim 10^{-10}$, BR($t \to c\gamma$) $\sim 10^{-12}$, BR($t \to cZ$) $\sim 10^{-13}$ and BR($t \to cH$) $\sim 10^{-14}$. Any observation of charged Higgs decay mode or FCNC decays of the top quark would be an evidence for the new physics beyond the Standard Model.

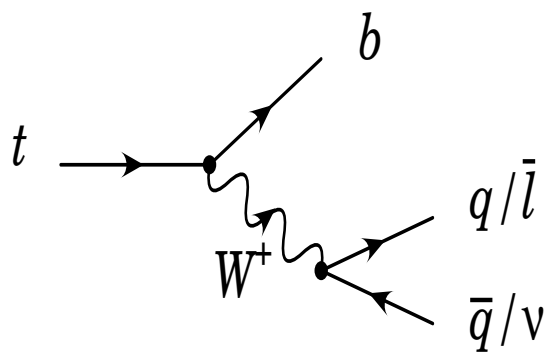

Figure 2.12: The Standard Model decay of the top quark.

It should be noted that it is not only the large mass of the top quark which gives it its short lifetime, but also the fact that the decay of t to b is not CKM suppressed.

2.6 Experimental Signature

This dissertation focuses on the Standard Model decay of the top quark ($t \to W^+b$) (Figure 2.12). The daughter b quark fragments and hadronizes to form a jet of final state particles and the W boson decays into fermions pairs $l\nu_l$ or $q\bar{q}$ (where l can be e or μ or τ and $q\bar{q}$ can be $u\bar{d}$ or $c\bar{s}$). In LO QCD, the branching ratios of W [93] into leptons and quarks are $\frac{1}{3}$, but quark decay modes get a factor of 3 enhancement because of color. For the purpose of experimental analysis, the top quark decay channels are classified using the decay modes of the W boson. In the case where $V_{tb} = 1$, the top quark will decay 100% of the time to b quark. Thus each $t\bar{t}$ event will have two b quarks and two W bosons. The decay channel classification is summarized in Table 2.2 and the relative branching fractions are shown in the Figure 2.13.

For data analysis, a $t\bar{t}$ event is classified into three broad categories which can be further subdivided by looking for semi-leptonic b quark decay involving soft e's and μ's. The latter technique is known as soft lepton b tagging.

1. The *alljets* Channel:

These are the events in which both the W's decay hadronically. The final state signature of an alljets event is six or more jets, where 2 jets come from the b decay and 4 jets come from the W decays. There may also be additional jets from the initial/final state radiation. Missing transverse energy ($\not{E}_T$) is not present at parton level but can arise from the mis-measurements of the energy in the event.

		$W \to e\nu_e$ (1/9)	$W \to \mu\nu_\mu$ (1/9)	$W \to \tau\nu_\tau$ (1/9)	$W \to q\bar{q}$ (2/3)
$W \to q\bar{q}$	(2/3)	12/81 $(e + jets)$	12/81 $(\mu + jets)$	12/81 $(\tau + jets)$	36/81 (all jets)
$W \to \tau\nu_\tau$	(1/9)	2/81 $(e\tau)$	2/81 $(\mu\tau)$	1/81 $(\tau\tau)$	
$W \to \mu\nu_\mu$	(1/9)	2/81 $(e\mu)$	1/81 $(\mu\mu)$		
$W \to e\nu_e$	(1/9)	1/81 (ee)			

Table 2.2: Decay modes and their branching fractions for a $t\bar{t}$ pair. Note that all the branching fractions are calculated assuming $V_{tb} \simeq 1$.

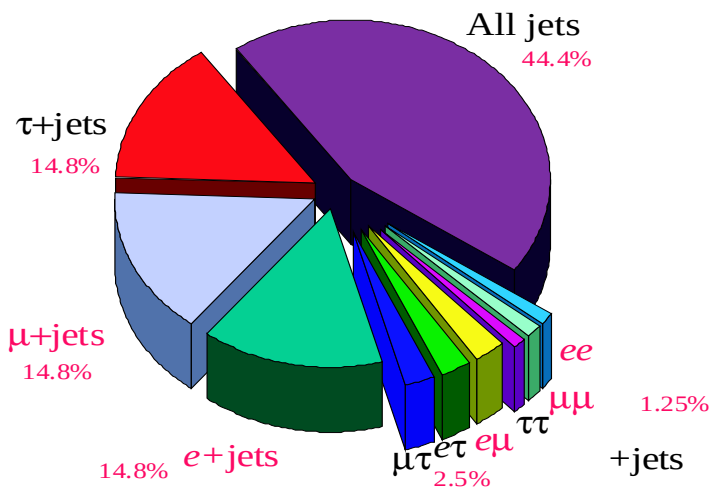

Figure 2.13: A pie chart showing the relative cross sections for various decay channels of a $t\bar{t}$ pair.

This is the channel with the largest branching ratio ($\simeq 44\%$) but it suffers from the difficulty of enormous background from QCD multijet events.

2. The $leptons + jets$ **channel ($l+$ jets):**

These are the events in which one W boson decays into leptons ($e\nu_e$ or $\mu\nu_\mu$

or $\tau\nu_\tau$) and the other into quarks. The final state signature is one high p_T lepton (e or μ or τ), four or more jets (2 from b quark decay and 2 from W decay) and missing transverse energy ($\not{E}_T$) from the presence of the undetected neutrino in the event. As with the alljets case there may be additional jets from the initial/final state radiation. Each of the three l + jet channels has a branching fraction of about $\simeq 15$ % . There is some enhancement in the e + jets and μ + jets channels through τ + jets events in which the τ has subsequently decayed to e or μ. The main background comes from inclusive W boson production with associated jets. There is also contribution from QCD multijet events, mainly from $b\bar{b}$ production, in which one b decays to a lepton and the associated jet is not reconstructed correctly.

3. The *dilepton* Channel:

These are the events in which both the W's decay leptonically giving ee, $\mu\mu$, $\tau\tau$, $e\mu$, $e\tau$, $\mu\tau$ final states. The signature of a dilepton event is: two high p_T leptons, two (or more) jets and missing transverse energy from the neutrinos in the event. Events in which the leptons are of the same type (ee, $\mu\mu$ and $\tau\tau$) have a branching fraction of 1.25% and the events in the leptons are of distinct type ($e\mu$, $e\tau$ and $\mu\tau$) have a branching fraction of about $\simeq 2.5$ %. The τ channels are not directly observed but they contribute to the ee, $\mu\mu$ and $e\mu$ channels via the leptonic decays of the τ. Since each event contains at least two neutrinos, unlike the alljets and the lepton+jets events, events in the dilepton channels can not be fully reconstructed by the detector. Experimently, the dilepton channels are the cleanest of the top quark decay channels because of the small backgrounds.

2.7 The $e\mu$ Channel

Figure 2.14 shows the schematic diagram for the $t\bar{t} \to e\mu$ channel. This is the focus of this thesis. In the following section we summarize the characteristics of the signal events and then go on to discuss possible backgrounds from physical and instrumental effects.

2.7.1 Signal Characteristics

An $e\mu$ dilepton candidate consists of an event in which one of the W bosons has decayed to give $e\nu_e$ and other $\mu\nu_\mu$. Thus the experimental signature is:

- 1 large transverse energy electron (E_T^e) - from $W \to e\nu_e$ decay
- 1 large transverse momentum muon (P_T^μ) - from $W \to \mu\nu_\mu$ decay
- Missing transverse energy ($\not{E}_T$) - from the two neutrinos

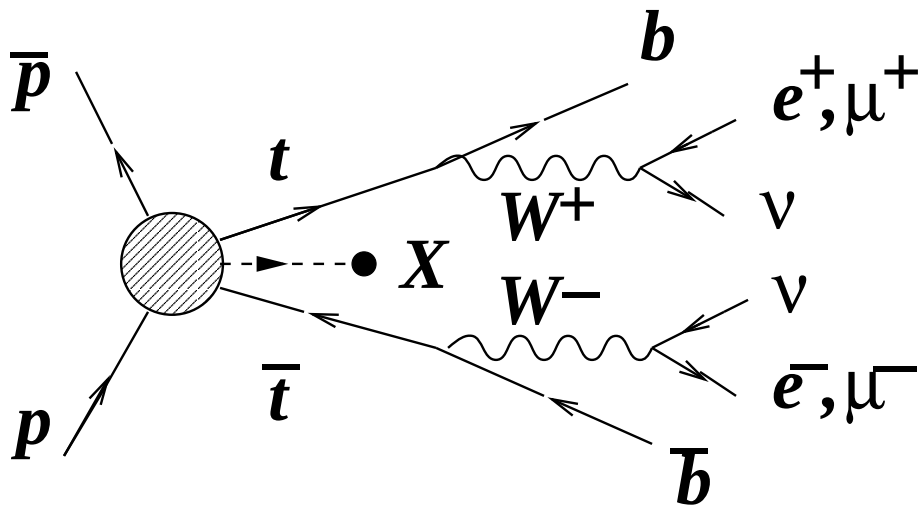

Figure 2.14: Schematic of the $t\bar{t} \rightarrow e\mu$X decay.

- $\geq$ 2 jets - from the fragmentation of the two b quarks (and initial/final state radiation)

The direct branching fraction for $t\bar{t} \rightarrow b\bar{b}WW \rightarrow e\nu_e\mu\nu_\mu$ + jet jet is 2.47 %. This is increased by an additional 0.96 % when the contributions from $t\bar{t} \rightarrow l\tau \rightarrow e\mu$ decays are included (where l can be e or μ or τ). However, the detection and reconstruction efficiencies for the τ events are somewhat smaller because the transverse energy (momentum) spectrum for the $e(\mu)$ from a τ decay is softer than those from the direct W decay and the presence of additional neutrinos leads to a decrease on the total missing transverse energy ($\not{E}_T^{cal}$).

2.7.2 Backgrounds

The background processes to the $e\mu$ channel can be divided into two main categories: physical and instrumental. These are discussed below.

Physical Backgrounds

These are the result of processes which lead to final state containing an electron and a muon with $\not{E}_T^{cal}$ and jets. These can mimic the signatures of top quark decay into $e\mu$ channel. The most significant of these are discussed below.

1. Z + jets production

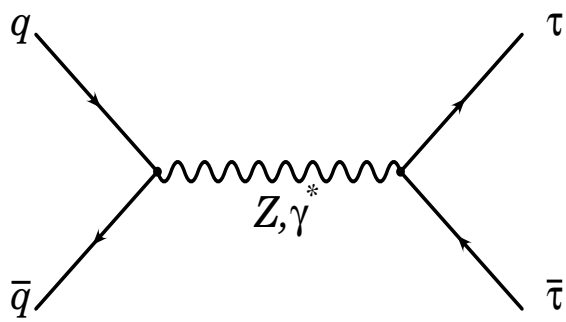

Figure 2.15: Lowest-order diagram for $\tau^+\tau^-$ production with Z or γ^* propagator.

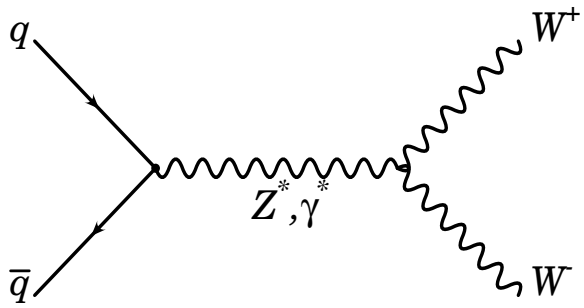

Figure 2.16: Lowest-order diagram for the Drell-Yan production of WW pairs.

The inclusive production of a Z boson with associated jets can be a source of background to $t\bar{t} \to e\mu$ events. Here the Z boson decays into $\tau^+\tau^-$ and taus further decay to give the e and μ. The Feynman diagram for the leading order production of $Z \to \tau\tau$ is shown in the Figure 2.15. The jets in these events are typically produced through radiative processes and have smaller transverse energies than those from the b jets in the top events. The production cross section of $Z \to \tau\tau \to e\mu$ is ≈ 12 pb (see appendix in [58]) which is significantly larger than the $t\bar{t} \to e\mu$ cross section. While the kinematics and topology can be use to suppress these events, they still provide significant background.

2. Drell-Yan $\tau^+\tau^-$ pair production

The Drell-Yan production of $\tau^+\tau^-$ pairs is also a source of a background. As with the $Z \to \tau^+\tau^-$ decay case, the $\tau\tau \to e\mu$ decay can mimic the signatures of a top quark event. The lowest-order Feynman diagram for this process is shown in Figure 2.15. The jets here are also produced through radiative processes and

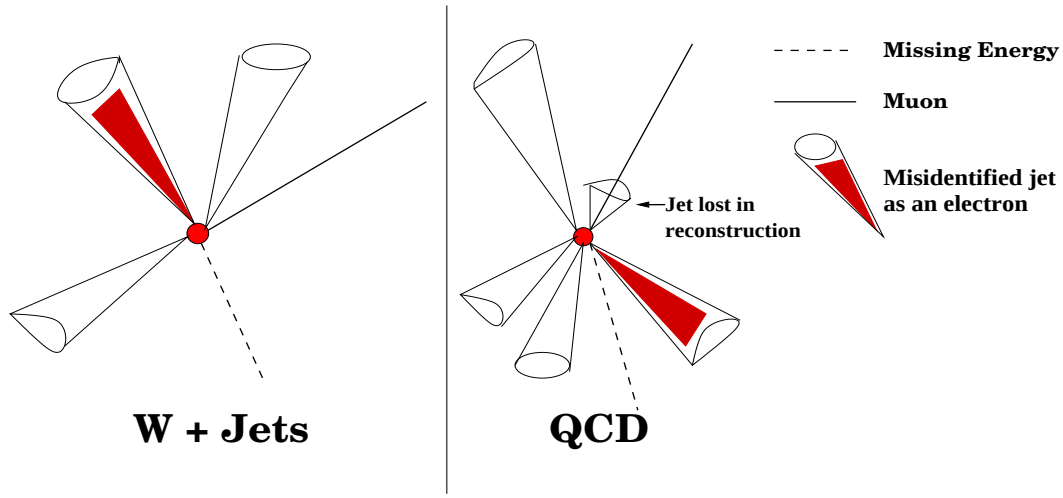

Figure 2.17: Cartoon of the instrumental fakes for W+jets and QCD events, where at least one jet in the event is misidentified as an electron.

have smaller transverse energies. Further suppression can be achieved by using the transverse energy spectra of the e (μ), which is even softer than that from $Z \to \tau\tau \to e\mu$. The cross section for this process is $\approx$ 6 pb [75].

3. WW pair production

The WW pairs are produced at the Tevatron through Drell-Yan process (See Figure 2.16). The final $e\mu$ state comes directly from the decays of the two W bosons. There is also a small contribution from the $W \to \tau\nu_\tau$ decay with a sequential $\tau \to e(\mu)\nu\bar{\nu}$ decay. The production cross section for $p\bar{p} \to W^+W^-$ at the Tevatron is $\approx$ 10 pb [36]. The branching fractions of $WW \to e\mu$ (including τ decays) is 3.43% so that the production cross section for the $e\mu$ final state is about 0.34 pb. Also, like other Drell-Yan processes, the jets in these events are produced by radiative processes and the E_T spectra are softer. However in terms of lepton final state, the transverse energy spectra of leptons are identical to those of $t\bar{t}$ events.

Instrumental Backgrounds

There are some backgrounds which are the results of instrumental effects in the detector and arise from the misidentification of jets as electrons. These can be conveniently separated into two categories depending on the source of the muon in the events.

1. W+jets production

The production of W + jets events is one of main sources of instrumental background. The measured production cross section for $p\bar{p} \to W\mathrm{X} \to \mu\nu\mathrm{X}$ is $\approx$ 2.42

nb [37]. If one of the associated jets is misidentified as an electron (Figure 2.17), then the final state can mimic the $t\bar{t} \rightarrow e\mu$X signature.

2. $b\bar{b}$ and $c\bar{c}$ production (QCD multi-jet processes)

This background is related to the production of QCD jets (mainly $b\bar{b}$ and $c\bar{c}$). The heavy quark (b or c) can have a semi-leptonic decay to a muon and may transfer all (most) of its energy to the muon, leaving little energy to hadronize. Such jets can easily be missed in reconstruction. If one of the other jets in the event is misidentified as an electron, then the final state would be one electron (misidentified jet), one muon (from b or c decay) and sufficient missing transverse energy (from mis-measurement). This is shown schematically in Figure 2.17. Despite heavy suppression from kinematical and topological constraints, this background can still be a source of significant problem because of the large $b\bar{b}$ and $c\bar{c}$ cross sections [38].

Chapter 3

Experimental Apparatus

Science clears the fields on which technology can build.

- Werner Heisenberg

This chapter gives a brief description of the experimental apparatus used in this study. In order to detect the particles produced in the collisions of protons and anti-protons, it is necessary to build a detector system around the collision point. One such detector, DØ, is located at one of the two collision points on the Tevatron ring located at Fermilab, Illinois.

3.1 The Tevatron, a particle accelerator

To reach the collision point inside the DØ detector the particle beams go through seven different parts of the Fermilab accelerator complex. These are: a Cockroft-Walton accelerator (pre-accelerator), the Linac (linear accelerator), the Booster synchrotron, the Main Ring, the Anti-proton Source, the Anti-proton Debuncher and the Tevatron Ring. Figure 3.1 shows the location of each part of the complex.

The source of the protons is hydrogen gas. This interacts with a hot cesium cathode to produce H^- ions. The ions are electro-statically accelerated by the Cockroft-Walton preaccelerator to an energy of 750 KeV and injected into the linac. Here, high radio frequency cavities accelerate the ions to an energy of 200 MeV. The H^- ions are then passed through a carbon foil which strips two electrons from the ion to create a beam of protons (H^+).

The next stage in the acceleration process is done by a 151 m diameter synchrotron, called the Booster. Synchrotron typically consists of three major parts: RF (radio-frequency) cavities, bending magnets, and focusing/defocusing magnets. The alternating high voltages of the RF cavities accelerate the beams of charged

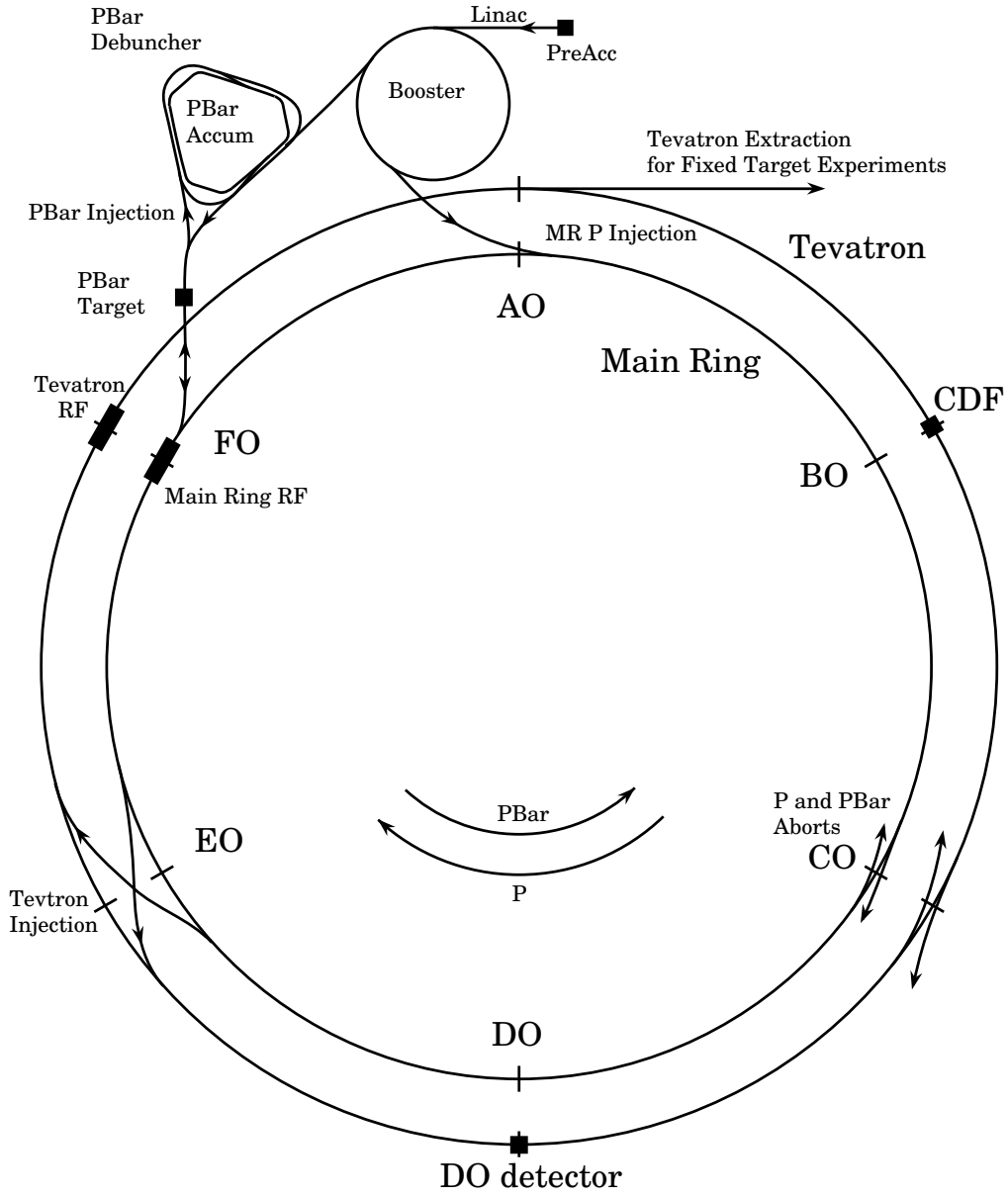

Figure 3.1: Schematic of the Fermilab accelerator complex.

particles every time they pass through the cavities and synchronize them with the RF frequency. Dipole magnets are used to bend the orbit of the beam by the Lorentz force exerted on charged particles moving in the magnetic field. Alternate quadrapole magnets are used to keep the beam focused in both transverse and longitudinal directions to ensure its stability and maintain high particle density. Protons

travel roughly 20,000 orbits inside the Booster as their energy is incremented up to 8 GeV. The booster repeats its cycle 12 times in rapid succession, delivering twelve pulses or bunches of protons for injection into the Main Ring.

The main ring is a proton synchrotron with a circumference of $\approx$ 6 km. It consists of a string of 774 conventional magnetic dipoles, 240 quadruples and 18 RF cavities. Once the protons have been injected into the main ring, they are accelerated to 150 GeV and then injected into the Tevatron Ring. The second task of the Main Ring is to generate 120 GeV protons, which can be extracted and used to generate anti-protons. The Main Ring beam pipe passes through the upper part of the DØ detector and proton losses can give rise to spurious signals in the detector. For this reason, events are not recorded during the time when main ring is active.

For anti-proton production, a 120 GeV proton beam extracted from the Main Ring is directed onto a nickel (or copper) target. The collisions produce a large quantity of secondary particles including anti-protons. These are selected from the other collision products by a series of magnets and transfered to the Debuncher ring. Here they are cooled and subsequently transferred to the Accumulator ring for beam storage and further cooling.

Accelerator radius	1000 m
Maximum beam energy	900 GeV
Injection energy	150 GeV
Peak luminosity	$\approx 2 \times 10^{31}$ cm^{-2} s^{-1}
Number of bunches	6 p, 6 $\bar{p}$
Intensity per bunch	$\approx 10^{11} p$, $\approx 5 \times 10^{10} p\bar{p}$
Crossing angle	0^0
Bunch length	50 cm
Transverse beam radius	$\approx$ 25 μm
Fractional energy spread	0.15×10^{-3}
RF frequency	53 MHz
$\bar{p}$ stacking rate	$\approx 3.5 \times 10^{10}$ per hour
Beam crossing frequency	290 kHz
Period between crossings	3.5 μs

Table 3.1: Parameters of the Fermilab Tevatron collider for Run 1 (1992-1996).

The Debuncher was designed to increase the density of anti-protons using two cooling techniques. The first of these, debunching uses a computer-coded RF

voltage to speed up slower anti-protons and slow down the faster ones. The second technique, known as stochastic cooling, reduces the transverse movement of the anti-protons. Here, the particles deviated from the central orbit are detected by sensors, and signals are passed to kicker electrodes which correct the particles trajectories.

The anti-protons from the debuncher are sent to a concentric ring called the Accumulator for further cooling and beam accumulation. It takes several hours to store the hundreds of billions of anti-protons needed for injection into the Main Ring.

The Tevatron Ring is a synchrotron made from the super-conducting magnets and is located 25 cm below the Main Ring in the same accelerator tunnel. It consists of 1000 super-conducting magnets operating at liquid helium temperature ($\simeq 4.6K$) which allows acceleration of the protons/anti-protons up to 900 GeV. 150 GeV bunches of the protons are transferred from the Main Ring to the Tevatron. The anti-protons are transferred from the Accumulator to the Main Ring, accelerated upto 150 GeV and then transferred to the Tevatron on an orbit in the opposite direction to the protons. During Run I, the Tevatron was operated with six proton and six anti-proton bunches spaced by about 3.5 μs. Both beams are accelerated to 900 GeV giving a center-of-mass energy of 1.8 TeV for $p\bar{p}$ collisions. The luminosity is increased by focusing the beams with super-conducting quadrapole magnets which are located near the interaction region. The beam spot has $\sigma_{x,y} \approx 40\mu$m and $\sigma_z \approx$ 30 cm.

A summary of the Tevatron operation parameters for Run I are listed in the Table 3.1. For a more detailed discussion of the accelerator the reader is referred to references [39, 40].

3.2 The DØ Detector

The DØ detector is a multipurpose facility designed to study high mass states and large P_T phenomena in the $p\bar{p}$ collisions [40]. Some of the physics goals were: the search for the top quark, precision studies of the W and Z bosons to test of the electroweak part of the Standard Model, studies of perturbative QCD, the production of b-quarks and the search for evidence of new phenomena beyond the Standard Model. The main features of the detector are good electron and muon identification capabilities, and finely segmented calorimetry which results in good measurements of electrons, photons, jets and missing transverse energy ($\not{E}_T$).

The detector consists of three main subsystems: the central tracking system, the calorimeters, and the muon spectrometers. A cut-away isometric view is shown in the Figure 3.2. Before proceeding to a discussion of the detector, it is useful to review the coordinate system and angle conventions used in the DØ experiment.

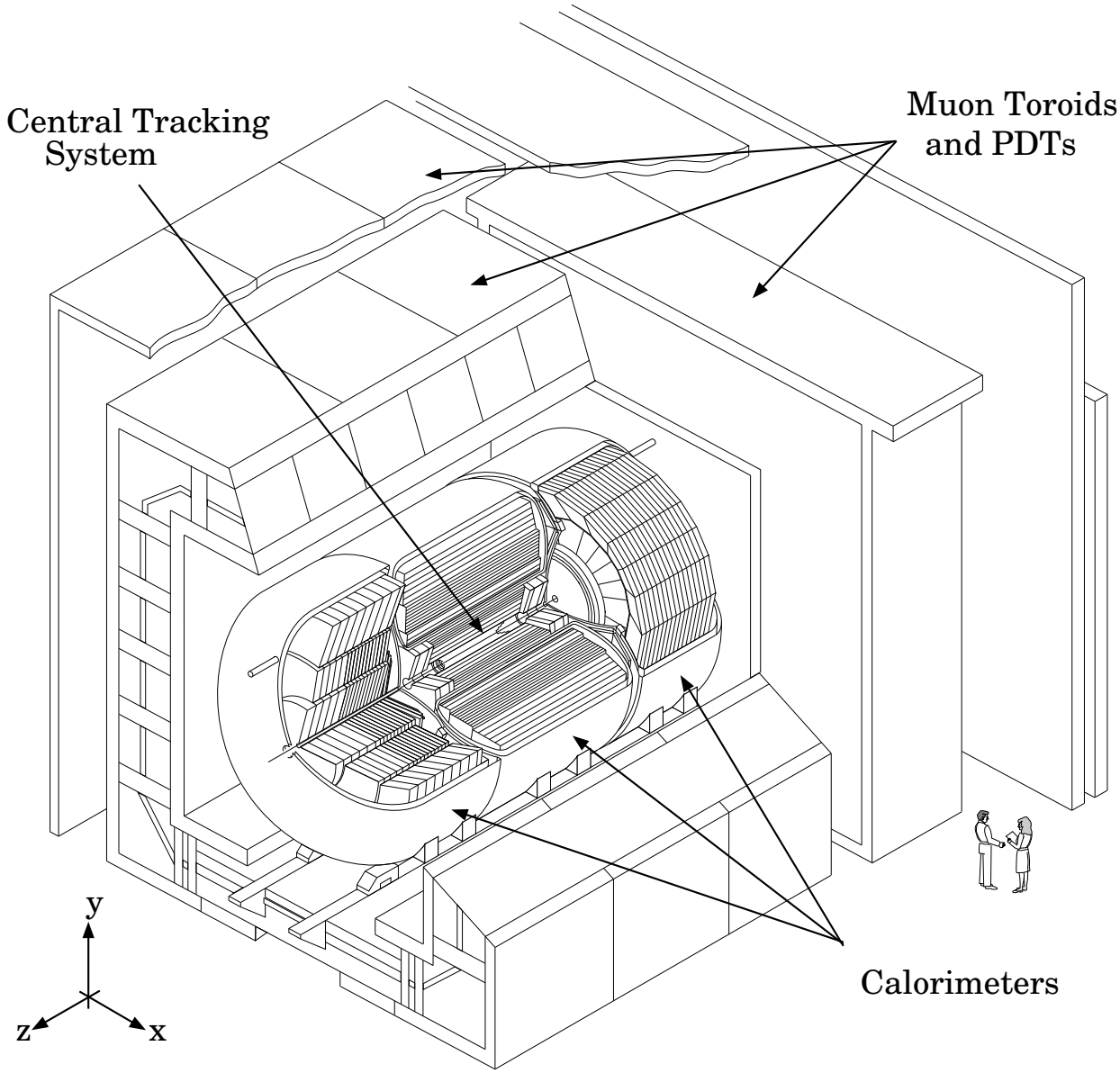

Figure 3.2: A cut-away isometric view of the DØ detector.

3.2.1 The DØ Coordinate System

DØ uses a right-handed coordinate system, where the z axis coincides with the beam-line and the positive x direction is defined as the direction of the proton beam. The x and y axes are then defined as the horizontal and vertical directions respectively (see Figure 3.3). The azimuthal angle (ϕ) is measured with respect to the $+x$ direction, and the polar angle (θ) is measured with respect to the $+z$ direction. The polar angle (θ) can be mapped to a more convenient coordinate

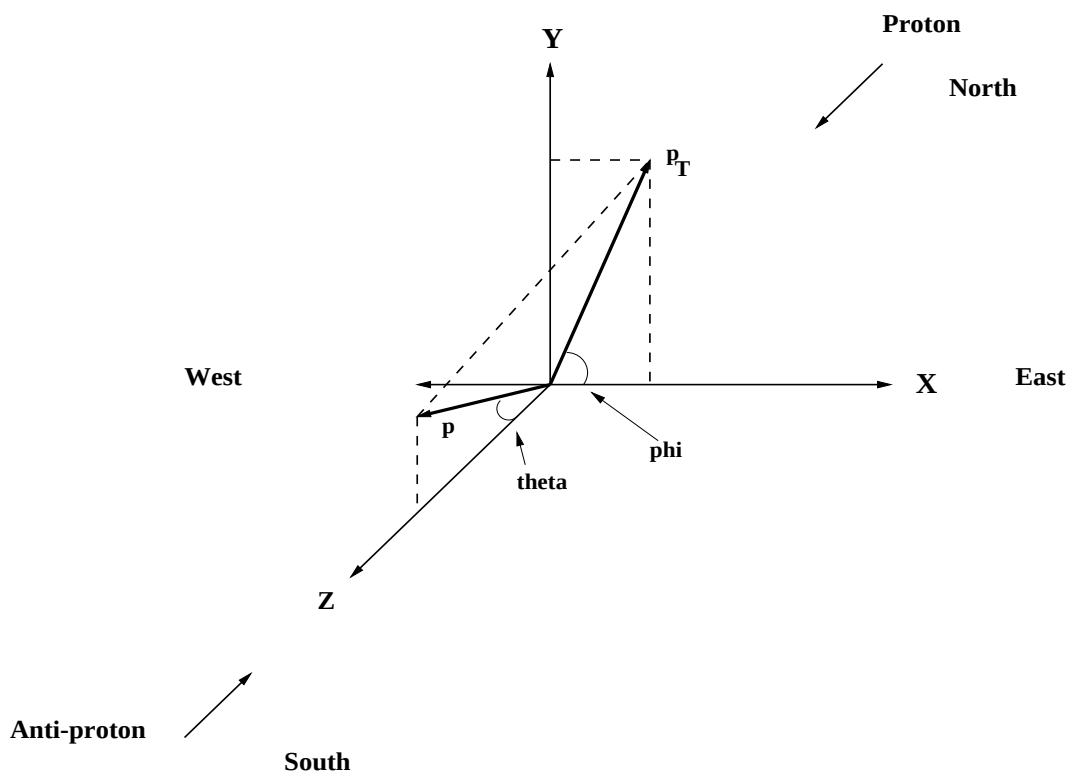

Figure 3.3: The DØ coordinate system.

called pseudorapidity (η) which is defined as

$$\eta = -\ln\left[\tan\left(\frac{\theta}{2}\right)\right] \tag{3.1}$$

In the high energy limit $m/E \to 0$ and η approaches the true rapidity (y) of the particle:

$$y = \frac{1}{2}\ln\left(\frac{E+p_z}{E-p_z}\right) \approx \eta \tag{3.2}$$

Rapidity is a useful quantity because it is invariant under longitudinal Lorentz boosts. Also, in many processes the differential cross sections are constant in rapidity. For example, in minimum bias events the quantity $\mathrm{dN/d}\eta \approx$ constant.

It is often convenient to express polar angles in the detector rest frame denoted η_{det} which is computed with respect to $x = y = z = 0$. In practice, the interaction point is characterized by a Gaussian distribution centered at $z \approx 0$ with $\sigma_z \approx 30$ cm, so that η and η_{det} may differ slightly for a given particle.

3.2.2 The Central Detector

The purpose of the central detector is to measure the trajectories of the charged particles coming out from the interaction point and determine the position of the interaction vertex (collision point). The central detector system of the DØ detector has no magnetic field so momentum information is not available at this stage. Figure 3.4 shows a schematic of the system indicating the positions of the various sub-systems. These are the vertex drift chamber (VTX), the transition radiation detector (TRD), the central drift chamber (CDC) and the two forward drift chambers (FDC).

A drift chamber consists of an enclosed volume filled with gas and arrays of anode and cathode wires. These create regions of approximately uniform electric field in the gas which acts as the ionization medium. When a charged particle passes through the chamber, the electrons produced in the ionization are drawn to the anode wires and create a signal pulse on the wire. By measuring the time taken to collect the charge (drift time) and the spatial position of the hit wire, the particle position can be determined.

The concept of the TRD is derived using the principles of electrodynamics [41]. A relativistic charged particle emits light when it passes through a junction between two dielectric media. The TRD utilizes this information to distinguish between charged pions and electrons.

The length of the central detector is 270 cm and its radius is 78 cm. It provides charged particle tracking in the region $|\eta| < 3.2$ with good spatial resolution of individual particles and a good determination of the ionization (dE/dx)

Vertex Chamber (VTX)

The vertex chamber is the innermost part of the tracking detector. It is a jet topology drift chamber whose inner and outer radii are 3.7cm and 16.2 cm respectively [40]. It consists of three layers of concentric cells with 110 cm wires oriented parallel to the beam axis. The innermost layer has 16 cells in azimuth and the outer two layers have 32 cells each. Figure 3.5 shows the cell geometry in the plane transverse to the beam direction (r, ϕ). The sense wires are staggered by $\pm 100\mu$m to resolve left-right ambiguities. The principle design and operating parameters of the vertex chamber are listed in the Table 3.2.

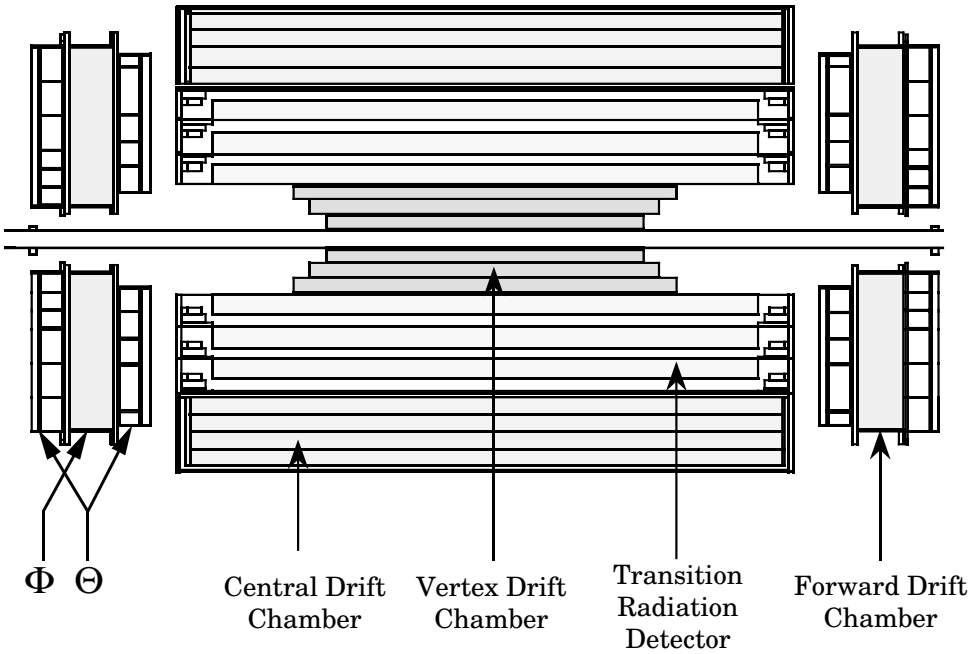

Figure 3.4: A side view of the DØ central tracking system.

Transition Radiation Detector (TRD)

The TRD is located in the space between the VTX and the CDC. It is used to provide electron identification independent of the calorimeter. When highly relativistic charged particles ($\gamma > 10^3$) traverse boundaries between media with different dielectric constants, transition radiation X-rays are produced on a cone with an opening angle of $1/\gamma$. Thus, the energy flux of the radiation is proportional to the γ of the particle. The DØ TRD consists of three separate modules, each of which contains a radiator and an X-ray detection chamber. The X-ray energy spectrum is determined by the thickness of the radiator layers and the gaps between the radiator layers.

Each of the modules contains 393 dielectric (polypropylene) foils with a mean gap of 150μm located in a gaseous nitrogen volume. Proportional drift wire chambers are used to convert the X-rays and the resulting charge is radially drifted to sensor wires for readout. Both magnitude and the arrival time of charge are used to distinguish electrons from hadrons.

Central Drift Chamber (CDC)

The central drift chamber sits between the TRD and the central calorimeter and is used to detect tracks at large angles. The CDC is a cylindrical shell of length 184 cm with a radial coverage from 49.5 cm to 74.5 cm and provides coverage for

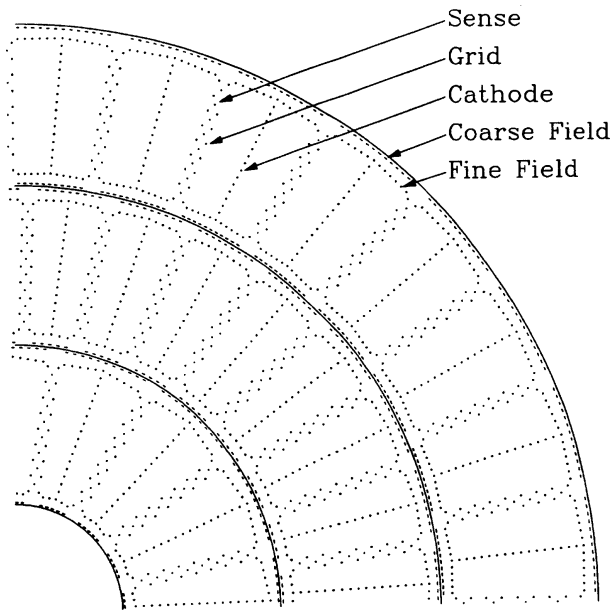

Figure 3.5: A rϕ view of one quadrant of the VTX detector

Length of the active volume:	Layer 1	96.6 cm
	Layer 2	106.6 cm
	Layer 3	116.8 cm
Radial interval (active)		3.7 - 16.2 cm
Number of layers		3
Radial wire interval		4.57 mm
Number of sensor wires/cell		8
Number of sensor wires		640
Gas composition		CO_2(95%)-ethane(5%)-H_2O(0.5%)
Gas pressure		1 atm
Drift field		1.0-1.6 kV/cm
Average drift velocity		7.6-12.8 μm/ns
Gas gain at sense wires		4x10^4
Sense wire potential		+2.5 kV
Sense wire diameter		25 μm NiCoTin
Guard wire diameter		152 μm Au-plated Al

Table 3.2: The operating parameters of the VTX chamber.

$|\eta| < 1.2$. A schematic of the CDC is shown in the Figure 3.6. It consists of four concentric rings with 32 azimuthal cells per ring. Each cell contains 7 equally spaced tungsten sensor wires of a diameter 30 μm. The wires are parallel to the z-axis and read out at one end to measure the ϕ coordinate. Delay lines embedded in the inner and outer shelves of each cell are used to propagate the signals induced from the nearest neighboring anode wire. The z coordinate of a track is measured from the difference in the signal arrival times at the two ends. The resulting r-ϕ resolution is $\approx 180\,\mu$m and the z resolution is $\approx 3\,$mm. Table 3.3 gives a summary of some of the parameters of the CDC.

Forward Drift Chambers (FDC)

The forward drift chambers [40] are used to increase the coverage for charged particles up to $|\eta| < 3.1$. There are two FDC modules located at the either end of the central detector and just before the end-cap calorimeters. Each FDC consists of a Φ chamber sandwiched between two Θ chambers, as shown in Figure 3.7. The Φ modules has radial sense wires and measures the ϕ coordinate and Θ chambers measures the θ coordinate. The geometric composition of the FDC cells is different from that of the CDC, but the operating principle is similar. The FDC position resolution is about 200 μm in r-ϕ and 300 μm in r-θ. Table 3.4 lists the main operating parameters of a FDC.

3.2.3 The DØ Calorimeters

Because of the absence of a central magnetic field the energy measurements at the DØ experiment rely heavily on the calorimeter. This also plays an important role in the identification of electrons/photons/jets and muons as well as the determination of the transverse energy balance in the event.

In a calorimeter, there are two types of particle showers, electro-magnetic and hadronic. An electro-magnetic shower consist of a cascade of electrons, positrons, and photons produced by bremsstrahlung and e^+e^- pair production. High energy e^- or e^+ radiate photons as they travel through material, and the photons in turn create lower energy e^+e^- pairs. The number of particles increases exponentially until electrons reach the critical energy, at which point they lose the same amount of energy by radiation and ionization. After that, the number of particles decreases and their energies gradually dissipate through the process of ionization. Such a electro-magnetic shower has a short and narrow energy profile. The longitudinal development of the showers is characterized by the radiation length (X_0) of the calorimeter material, which is the the mean distance over which an electron loses all but $1/e$ of its energy by bremsstrahlung.

Hadronic showers are caused by the strong (nuclear) interactions between the hadrons and the nuclei of the calorimeter material. In such an interaction most of the energy is transferred to the nucleus resulting in the production of secondary

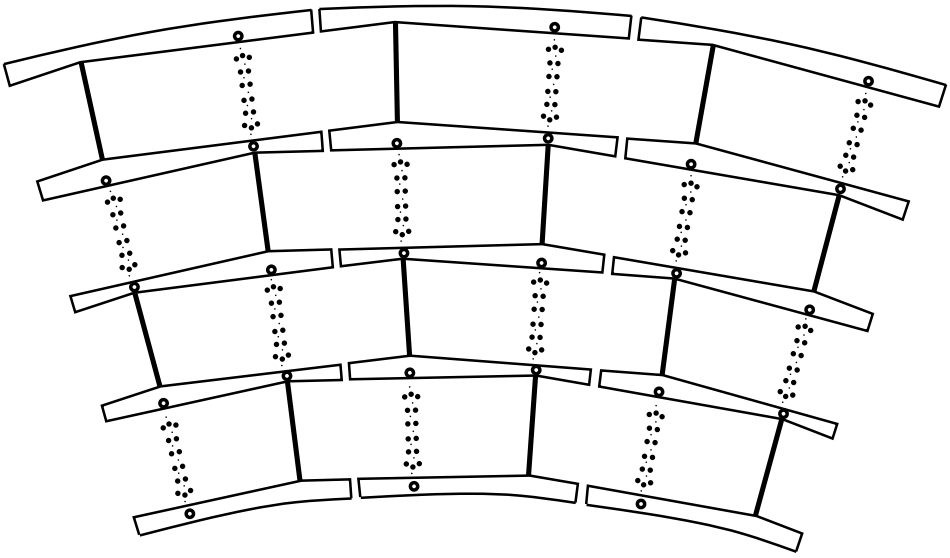

Figure 3.6: A end view of the 3 CDC modules.

Active volume length	179.4 cm
Active radial interval	51.8 - 71.9 cm
Number of layers	4
Radial interval between wires	6.0 mm
Number of sensor wires/cell	7
Number of sensor wires	896
Number of delay lines	256
Gas composition	Ar(93%)-CH_4(4%)-CO_2(3%)-H_2O
Gas pressure	1 atm
Drift field	620 V/cm
Average drift velocity	34 μm/ns
Gas gain in the sensor wires	$2,6 \times 10^4$
Sensor wire potential	+1.5 kV
Sensor wire diameter	30 μm Au-plated W
Guard wire diameter	125 μm Au-plated CuBe

Table 3.3: Some parameters of the CDC chamber.

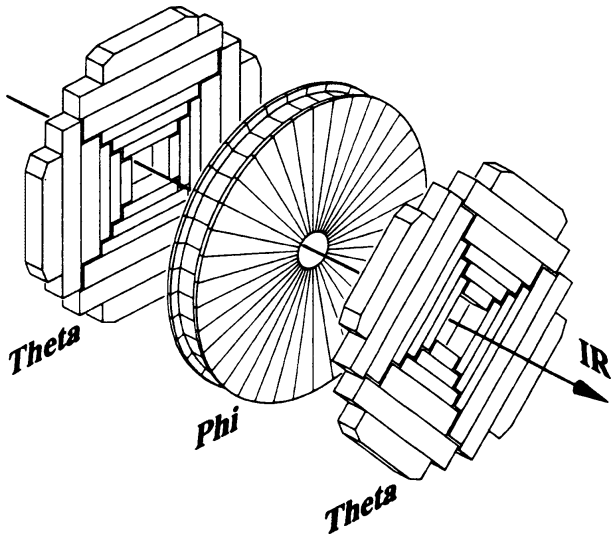

Figure 3.7: An exploded end view of the FDC.

	Θ *modules*	Φ *modules*
z interval	104.8-111.2 cm	113.0-127.0
	128.8-135.2 cm	
Radial interval	11-62 cm	11-61.3 cm
Number of cells per radius	6	
Maximum drift distance	5.3 cm	5.3 cm
Stagger of sense wires	0.2 mm	0.2 mm
Sensor wire separation	8 mm	8 mm
Angular interval/cell		10°
Number of sensor wires per cell	8	16
Number of delay lines per cell	1	0
Number of sense wires/end	384	576
Number of delay lines read out/end	96	
Gas mixture	Ar(93%)-CH_4(4%)-CO_2(3%)-H_2O	
Gas pressure	1 atm	1 atm
Drift field	1.0 kV/cm	1.0 kV/cm
Average drift velocity	37 μm/ns	40 μm/ns
Gas gain at sense wire	$2.3, 5.3 \times 10^4$	3.6×10^4
Sense wire potential	+1.5 kV	+1.5 kV
Sense wire diameter	30 μmAu-plated W	
Guard wire diameter	163 μm Au-plated Al(5056)	

Table 3.4: Forward drift chamber parameters.

hadrons, which in turn produce more hadrons. This cascade process begins to stop when the energies of the secondary hadrons are small enough to be exhausted by ionization or to be absorbed in a nuclear process. Hadronic showers tend to be wide and more penetrating than the electro-magnetic showers. The length scale appropriate for hadronic showers is the nuclear interaction length (λ_I) which is given very roughly by $\lambda_I \approx 35\ \mathrm{A}^{1/3}$ g cm^{-2}, where A is the atomic number o the material.

The DØ calorimeters [40] are of uranium-liquid argon sampling design. These consist of stacks of dense metallic plates which are used as energy absorber and the inter-plate gaps which is filled with some material to sample the ionization produced by electro-magnetic and hadronic showers. The DØ design uses liquid argon as the sensitive (sampling) material, and uranium (copper) as the absorber. Some of the advantages of this design are the unit gain of the liquid argon, the simplicity of calibration, the flexibility to segment the calorimeter in longitudinally and transversely, the radiation hardness and the relatively low unit cost for readout electronics.

The calorimeters (see Figure 3.8) are divided into three modules: the Central Calorimeter (CC), the North End Calorimeter (ECN), and the South End Calorimeter (ECS). Each module has an electro-magnetic section (EM) with 3mm uranium plates, a fine hadronic section with 6mm uranium plates and a coarse hadronic section with 4.7cm copper or stainless steel plates. To provide uniform coverage across the gaps between the cryostats, a scintillator counter known as the inter-cryostat detector (ICD) is used. This consists of an array of scintillator tiles and is located between the CC and EC cryostats. The EM section of the calorimeter is ≈ 21 radiation lengths deep, and is divided into four longitudinal layers for the study of shower depth profiles. The hadronic sections are 7 to 9 nuclear interaction lengths thick and are divided into four (CC) or five (EC) layers. The calorimeter transverse segmentation is 0.1×0.1 in $\Delta\eta \times \Delta\phi$ (see Figure 3.9) except for the third EM layer, where the maximum of electro-magnetic showers is expected, where the segmentation is 0.05×0.05. Figure 3.10 shows a typical unit cell of the calorimeter modules showing the liquid argon gaps, absorber plates, and signal boards.

Central calorimeter (CC)

The CC consists of three concentric cylindrical shells 226 cm in length with a radial coverage of $75 < r < 222$ cm and covers the pseudorapidity range $|\eta| \leq 1$. There are 32 EM modules in the inner ring, 16 fine hadronic (FH) modules in the surrounding ring and 16 coarse hadronic (CH) in the outer ring. In order to reduce the energy loss in cracks, the EM, FH, and CH module boundaries are arranged so that there are no cracks pointing at the interaction point. Table 3.5 summarizes the design specifications for the central calorimeter.

End Calorimeter (ECN, ECS)

There are two end calorimeters located at the north (ECN) and south (ECS) ends of the central tracking system (see Figure 3.8). Each calorimeter consists of one EM module (See Figure 3.11), one inner hadronic module (IH), and 16 middle

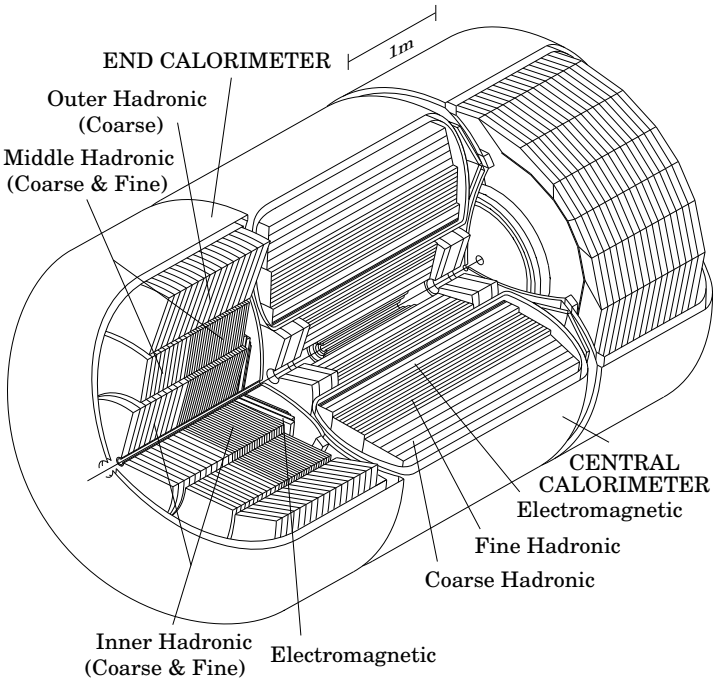

Figure 3.8: A cut-away view of the CC and EC calorimeters.

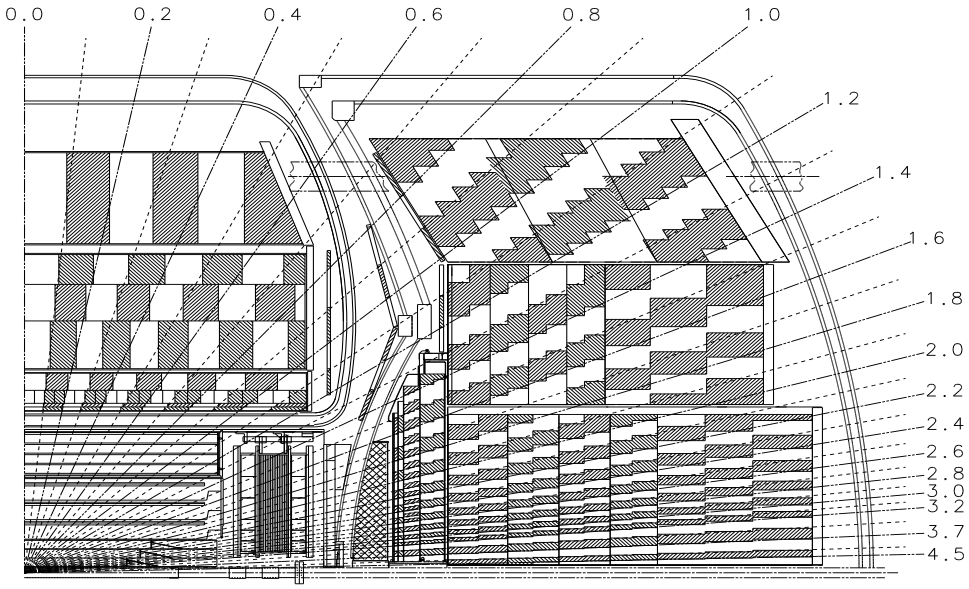

Figure 3.9: A schematic of one quadrant of the Calorimeters showing arrangement of cells and towers.

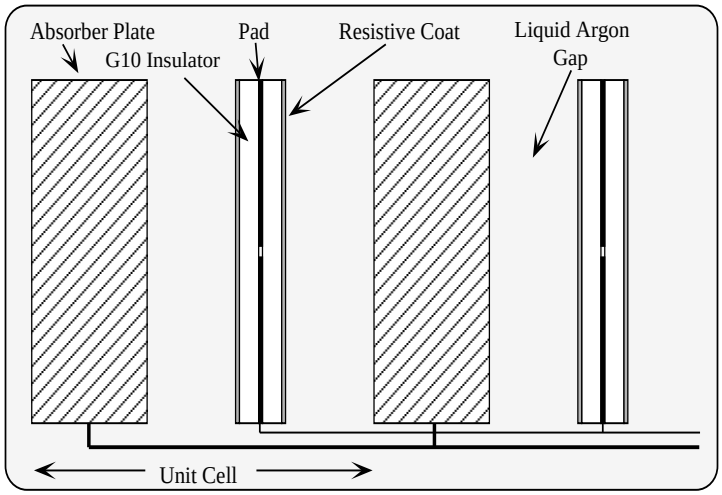

Figure 3.10: A calorimeter unit cell showing the arrangement of the absorber plate, argon gaps and readout boards.

	EM	FH	CH
Rapidity coverage	± 1.2	± 1.0	± 0.6
Number of modules	32	16	16
Absorber material	Depleted Uranium	Depleted Uranium (1.7% niobium alloy)	Copper
Absorber material thickness (cm)	0.3	0.6	4.65
Argón gap (cm)	0.23	0.23	0.23
Number of cells/module	21	50	9
Longitudinal depth	20.5 X_0	3.24 λ_0	2.93 λ_0
Number of readout layers	4	3	1
Cells/readout layer	2, 2, 7, 10	21, 16, 13	9
Total radiation length	20.5	96.0	32.9
Radiation length/cell	0.975	1.92	3.29
Total absorption length	0.76	3.2	3.2
Absorption lengths/cell	0.036	0.0645	0.317
Sampling fraction (%)	11.79	6.79	1.45
Segmentation ($\eta \times \phi$)	0.1 × 0.1 (3rd EM: 0.05 × 0.05)	0.1 × 0.1	0.1 × 0.1
Total number of readout cells	10,368	3,456	768

Table 3.5: CC design parameters.

and outer hadronic (MH and OH) modules. The ECEM transverse segmentation is identical to the CCEM, except that the third layer segmentation is 0.1×0.1 for $|\eta_{\rm det}| > 2.5$. The azimuthal boundaries of the MH and OH modules are offset to prevent projecting cracks. Some of the specifications of the end calorimeters are listed in the Table 3.6.

Inter-cryostat Detectors (ICD) and Massless Gaps (MG)

There is a substantial amount of material in the form of cryostat walls which lies in the region $0.8 \leq |\eta| \leq 1.4$. Two scintillation counter arrays, known as inter-cryostat detectors (ICD) are placed in this region to correct for the energy deposited by the particles in the uninstrumented cryostat walls. Each ICD consists of 384 scintillator tiles of size 0.1×0.1, exactly matching the segmentation of the calorimeter cells. In addition, separate readout cells called massless gaps (MG) are installed inside the CC and EC cryostats in the $0.8 \leq |\eta| \leq 1.4$ region. These consist of three liquid argon gaps and two readout boards with no absorber plates. The MG detectors together with the ICD provide an approximation to the sampling of EM and hadronic showers and provide close to uniform energy resolution in the CC-EC transition gaps.

Calorimeter Readout and Performance

There are $\sim$ 47000 readout channels in the DØ calorimeter. The signals from the modules are brought to charge sensitive pre-amplifiers which are mounted in enclosures on the surface of each cryostat by specially fabricated cables. The output signals from the pre-amplifiers are then transported to the baseline subtractor (BLS), shaping and sampling circuits. Depending on the signal size, the BLS outputs can be amplified by a factor of between 1 and 8 so as to reduce the dynamic range requirements of subsequent digitization. The BLS outputs are sent from the detector platform to the moving counting house (MCH).

The performance of the calorimeter has been studied by using electron and pion beams with energies between 10 and 150 GeV at a test beam facility [40, 42] . The energy resolutions are:

$$\frac{\sigma(E)}{E} = \frac{16\%}{\sqrt{E(GeV)}} \oplus 0.3\% \tag{3.3}$$

and

$$\frac{\sigma(E)}{E} = \frac{41\%}{\sqrt{E(GeV)}} \oplus 3.2\% \tag{3.4}$$

for electrons and pions, respectively. The position resolution of the calorimeter is important for identification of the electron backgrounds due to overlap of photons and charged particle tracks. This varies approximately as $\sqrt{E}$ and also varies between 0.8 and 1.2 mm over the full range of impact positions.

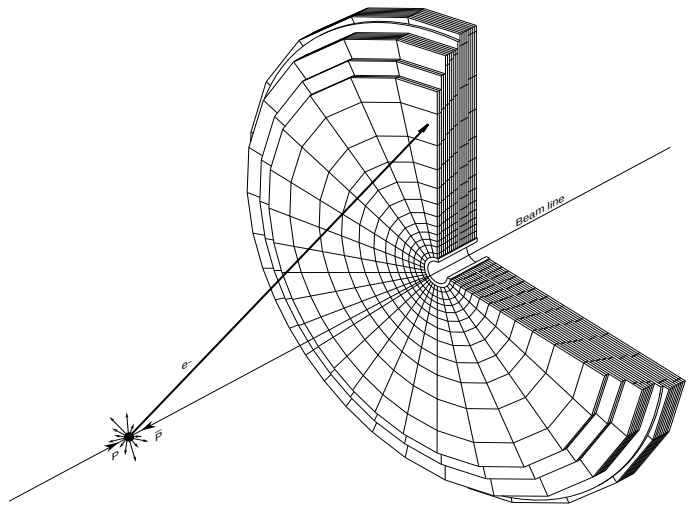

Figure 3.11: A view of the EC EM module.

	EM	IFH	ICH	MFH	MCH	OH
Rapidity coverage	1.3-4.1	1.6-4.5	2.0-4.5	1.0-1.7	1.3-2.0	0.7-1.4
Number of modules	1	1	1	16	16	16
Absorbing material[a]	U	U	SS[b]	U	SS	SS
Absorbent thickness (cm)	0.4	0.6	4.6	0.6	4.6	4.6
Argon gap (cm)	0.23	0.21	0.21	0.22	0.22	0.22
Number off cells/Module	18	64	12	60	12	24
Longitudinal depth	$20.5X_\circ$	$4.4\lambda_\circ$	$4.1\lambda_\circ$	$3.6\lambda_\circ$	$4.4\lambda_\circ$	$4.4\lambda_\circ$
Number of readout cells	4	4	1	4	1	3
Cells/readout layer	$2, 2, 6, 8$	16	12	15	12	8
Total radiation lengths	20.5	121.8	32.8	115.5	37.9	65.1
Total absorption lengths (Λ)	0.95	4.9	3.6	4.0	4.1	7.0
Sampling fraction (%)	11.9	5.7	1.5	6.7	1.6	1.6
Segmentation $\Delta\phi^c$	0.1	0.1	0.1	0.1	0.1	0.1
Segmentation $\Delta\eta^d$	0.1	0.1	0.1	0.1	0.1	0.1
Total readout channels	14976	8576	1856	2944	768	1784

Table 3.6: The design parameters of the ECN and ECS calorimeters.

[a]Depleted uranium. The absorbing material in modules FH (IFH and MFH) contains a 1.7% niobium alloy.

[b]Stainless steel

[c]The third layer of EM $\Delta\phi \times \Delta\eta = 0.05 \times 0.05$ for $|\eta| < 2.6$

[d]For $|\eta| > 3.2, \Delta\phi = 0.2$ $\Delta\eta \approx 0.2$

3.2.4 The Muon Spectrometers

Since muons are weakly interacting long lived particles they penetrate the detector material depositing little of their energy in the calorimeter as they pass through. The outermost part of the DØ detector consists of the wide angle (WAMUS) and small angle (SAMUS) muon spectrometers [43]. These consist of five toroidal magnets surrounded by proportional drift chambers (see Figure 3.13). The toroids provide magnetic fields ($\approx$ 2T) to bend the muon trajectory which is measured by the drift chambers. This system enables muon identification and measurement of trajectories down to approximately 3 degrees from the beam pipe. The total number of interaction length transversed by a muon varies with η (see Figure 3.12) but is typically $\geq 14X_o$.

Wide Angle Muon Spectrometers (WAMUS)

Each WAMUS consists of a toroidal magnet and three layers of proportional drift tube (PDT) planes (see Figure 3.13). The first layer (A) of PDT chambers is mounted in the inner surface of the magnetized toroids. The second and third layer (B and C) are mounted outside of the toroids and are separated by $\approx$ 1.4 m. The A layer consists of four planes of PDT's where as the B and C layers each have three planes. In the WAMUS spectrometers, the central toroid (CF) covers the pseudorapidity region $|\eta| \leq 1$ and two end toroids (EFs) cover $1 < |\eta| \leq 2.5$. Some other parameters of the WAMUS are summarized in the Table 3.7.

Small Angle Muon Spectrometers (SAMUS)

The small angle muon systems (SAMUS) consist of two toroids and sets of PDT's. The chambers cover the pseudorapidity region $2.5 \leq |\eta| \leq 3.5$ and are arranged into three stations A, B and C in the same manner as in the WAMUS spectrometers. Each layer consists of three doublets of proportional drift tubes oriented in x, y, and u (u being at 45° with respect to x and y) directions. Further details about the SAMUS are listed in Table 3.7.

3.2.5 Trigger and Data Acquisition

During data taking in Run 1 (1992-1996), the bunch crossing rate of the Tevatron was 290 kHz. At this frequency there are hundreds of thousands of collisions occurring per second within the DØ detector. It is impractical to read out the entire detector for all the collisions even if all the events were of the interest. In order to select the interesting events (at a rate of a few events per second) from such a large amount of collisions, we need a trigger and data acquisition system. The DØ detector has a four level trigger system with three hardware levels (Level Ø, Level 1, Level 1.5) and one software level (Level 2) [40]. These are summarized in the following sections.

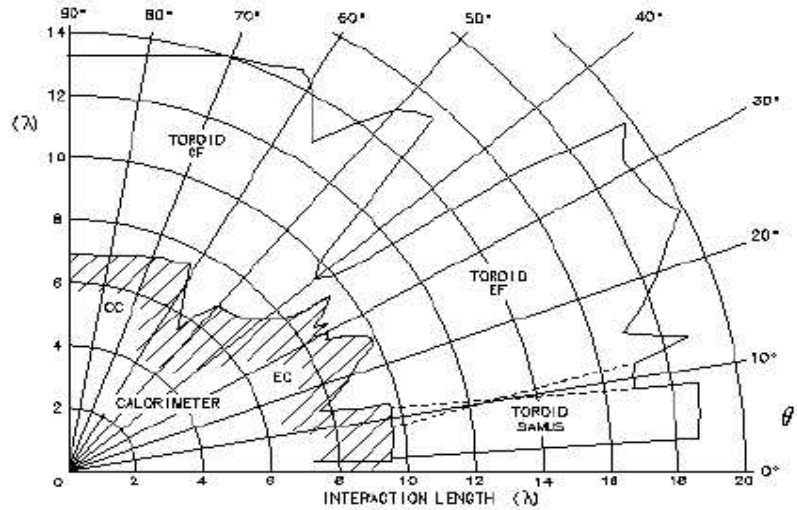

Figure 3.12: The nuclear interaction length of the DØ detector as a function of the polar angle (θ).

	WAMUS	SAMUS
Pseudorapidity coverage	$\lvert\eta\rvert \leq 1.7$	$1.7 \leq \lvert\eta\rvert \leq 3.6$
Magnetic field	2 T	2 T
Number of chambers	164	6
Interaction lengths	13.4	18.7
Bend view resolution	± 0.9 mm	± 0.35 mm
Non-bend (ξ) resolution	± 10 mm	± 0.35 mm
Gas composition	Ar 90%, CF_4 6%, CO_2 4%	CF_4 90%, CH_4 10%
Avg. drift velocity	6.5 cm/μs	9.7 cm/μs
Anode wire voltage	+4.56 kV	+4.0 kV
Cathode pad voltage	+2.3 kV	—
Number of cells	11,386	5308

Table 3.7: Muon System Parameters.

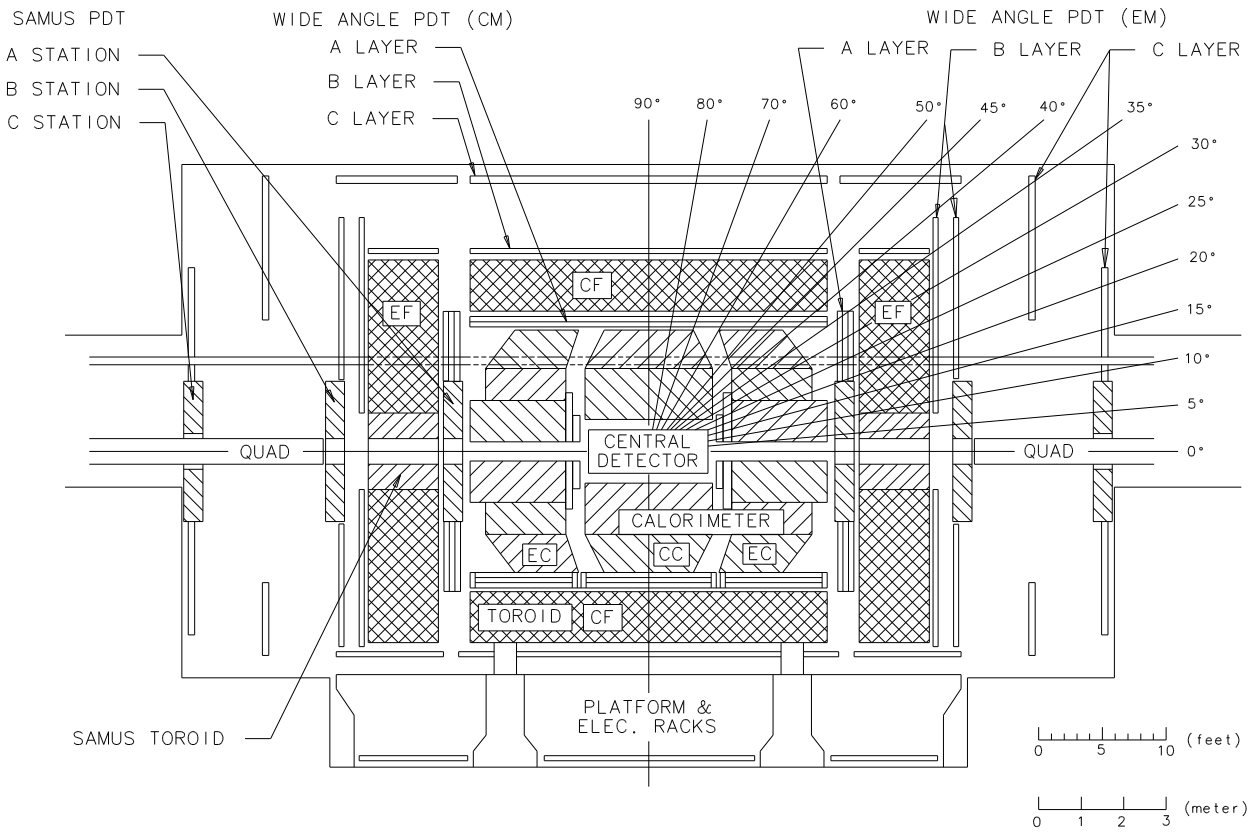

Figure 3.13: An elevation view of the DØ detector showing the muon system.

The Level Ø Trigger (LØ)

The Level Ø trigger indicates the occurrence of inelastic collisions and serves as the luminosity monitor for the experiment. It consists of two array of scintillator hodoscopes mounted between the FDC and EC calorimeters. The timing information from the LØ counters is used to determine the approximate interaction z position for subsequent trigger levels and the hit rates are used to monitor instantaneous luminosity. For example, a luminosity of $\mathcal{L} = 10^{30}$ cm^{-2}s^{-1} corresponds to a LØ rate of about 150 kHz.

The Level 1 (L1) and Level 1.5 (L1.5) Trigger

The Level 1 trigger elements collect the digital information from each of the detector sub-systems and flags an event for further examination. Many of the Level 1 triggers operate within the 3.5 μs time interval between beam crossings and contribute no dead-time. Others such as the muon trigger require several bunch crossing times to complete and are referred to as Level 1.5 triggers. The rate of successful Level 1 triggers is about 200 Hz.

The L1.5 is a DSP-based trigger and improves energy resolution by examining the energy in towers neighboring the L1 calorimeter EM towers. Additionally, energy sums are computed from adjacent hadronic towers, and the ratio E_{EM}/E is used for further background rejection. The rate is further reduced to 100 Hz using L1.5 trigger.

The Level 2 Trigger (L2)

The L2 trigger system is software-based and consists of a farm of 50 parallel VAX nodes connected to the detector electronics and triggered by a set of eight 32-bit high-speed (40 MB/s) data cables. The L2 nodes are coordinated through the host computer (see Figure 3.14). Event filtering is built around a series of filter tools each of which has a specific function related to a identification of a type of particle or event characteristic. These include tools for jets, muons, calorimeter EM clusters, track association with calorimeter clusters, $\sum E_T$ and missing $E_T(\not{E}_T)$. Other tools recognize specific noise or background conditions. The rate of successful Level 2 events is about 2 Hz.

The Main Ring Veto Triggers

The Main Ring passes through the course hadronic portion of CC and EC calorimeters. It is active during the production of the anti-protons and during new beam injection into the Tevatron. Beam loss from the Main Ring can cause spurious signals in the hadronic calorimeter and muon chambers. Typically this occurs once every 2.4 seconds when the protons are injected into the Main Ring and 300 ms later when the beam passes through transition [44]. A timing circuit linked to the Main Ring control system is used to set a hardware flag known as MRBS-LOSS. This is set every time the protons are injected and remains set for 400ms until the beam has passed through transition and muon system recovers. In addition, smaller beam losses occur with every passage of the beam. These are significant only if the